Nucleation of Brushite and Hydroxyapatite from Amorphous Calcium Phosphate Phases Revealed by Dynamic *in situ* Raman Spectroscopy

German Montes-Hernandez[a] * and François Renard[a, b]

[a] Univ. Grenoble Alpes, Univ. Savoie Mont Blanc, CNRS, IRD, IFSTTAR, ISTerre, 38000 Grenoble, France

[b] The Njord Centre, Department of Geosciences, University of Oslo, box 1048 Blindern, 0316 Oslo, Norway

*Corresponding author: Dr. German Montes-Hernandez

E-mail address: german.montes-hernandez@univ-grenoble-alpes.fr

1

Abstract

Since the 1970s, it is admitted that calcium phosphate crystals nucleate from one or several early amorphous calcium phosphate phases into several *in vivo* and *in vitro* systems. However, the precise chemical composition, structure and transformation mechanism of these amorphous phases remain controversial. Here, we characterize the reaction mechanism and kinetics of formation of two phosphate crystals, brushite and hydroxyapatite, by using *in situ* Raman spectroscopy in batch reactors at 25°C. We investigate three pH regimes to control the phosphate speciation in solution and used solutions with or without citric acid, a complexing agent that may stabilize the amorphous phases. As expected, brushite ($CaHPO_4.2H_2O$) forms at pH < 9.8. Amorphous calcium phosphate (ACP: $CaHPO_4.nH_2O$) with short lifetime (<2 minutes) and octocalcium phosphate (OCP: $Ca_8(HPO_4)_2(PO_4)_4.5H_2O$) are the main transient phases prior to brushite nucleation that occurs after ~8 minutes. At pH > 11, hydroxyapatite (HAp: $Ca_{10}(PO_4)_6(OH)_2$) nucleates after >35 minutes, depending on the experimental conditions. The reaction mechanism steps for hydroxyapatite are more complex compared to brushite. For hydroxyapatite formation, amorphous calcium phosphate phases with different chemical composition ($Ca(HPO_4)_{1-x}(PO_4)_{(2/3)x}.nH_2O$, with x in the range 0.2-1, and with different lifetime may form. Amorphous tricalcium phosphate (ATCP: $Ca(PO_4)_{2/3}.nH_2O$ or $Ca_3(PO_4)_2.nH_2O$ when x=1) is the most persistent phase which can transform either into OCP and then hydroxyapatite, or directly evolve into hydroxyapatite at pH > 12.2. The presence of citric acid retards the transformation kinetics by increasing the nucleation times of brushite and hydroxyapatite, but has little effect on the reaction mechanism steps. Finally, this study identifies new reactive pathways that characterize the formation of amorphous calcium phosphate phases and their transformation into brushite microcrystals or hydroxyapatite

2

nanocrystals under abiotic conditions, relevant to a wide range of technological applications and natural environments.

TOC Graphic
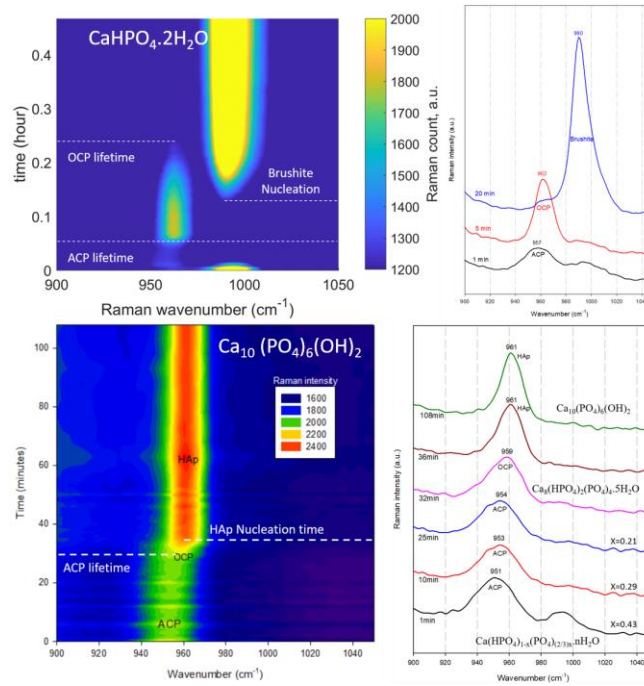
Synopsis: The nucleation of brushite and hydroxyapatite was monitored in real-time by Raman spectroscopy at 25 °C. For both minerals, amorphous calcium phosphate ($Ca(HPO_4)_{1-x}(PO_4)_{(2/3)x} \cdot nH_2O$) with different Raman signature instantaneously formed in the initial solution. Then, the amorphous phases transform into OCP, a crystalline transient phase. Finally, OCP transforms into brushite micro-crystals or into hydroxyapatite nanocrystals.

4

1. Introduction

Calcium phosphates (e.g. hydroxyapatite, brushite, octo-calcium phosphate and amorphous calcium phosphates) are critically important biogenic minerals constituting hard tissues (bones, teeth and cartilages) in vertebrates. Phosphorus (P) and calcium (Ca) are also essential elements for the development of living organisms. Moreover, calcium phosphates find wide medical and industrial applications in dentistry, orthopedics, reconstructive surgery, food additives, fertilizers, and water depollution (1-6). The formation of calcium phosphates and the interactions and associations of these minerals with organic macromolecules have been widely investigated under *in vivo* and *in vitro* conditions in the last decades (7-10) in order to identify the nature of first primary precipitating particles, their lifetime and their chemical transformation into other minerals in aqueous media (11-20). For example, the formation of hydroxyapatite nanocrystals $(Ca_{10}(PO_4)_6(OH)_2)$ under biotic or abiotic conditions involves the early formation of a transient amorphous calcium phosphate phase (ACP) (11-26). This phase may either (1) transform directly by a solid-state transformation, (2) dissolve and reprecipitate to produce nanocrystalline hydroxyapatite, or (3) nucleate inside other amorphous phases (e.g. 9, 11, 16, 18, 24). The first theory of phosphate formation from precursor amorphous phases was proposed by Posner and Betts (11) who observed pre-nucleation clusters of $Ca_9(PO_4)_6$ with a size close to ~1 nm (so-called 'Posner's cluster'). These authors proposed that the clusters not only could be the building blocks for ACP but also could play an important role during the transformation of ACP into hydroxyapatite, suggesting that ACP only dissociates into these clusters rather than undergoing a complete ionic dissolution (11, 16). However, the structure of pre-nucleation clusters during hydroxyapatite formation is still debated (e.g. 12-13, 25-26). For example, crystalline metastable

6

phases such as octo-calcium phosphate (OCP) ($Ca_8(HPO_4)_2(PO_4)_4.5H_2O$) and brushite ($CaHPO_4.2H_2O$) have been proposed to form as transient phases prior to hydroxyapatite (HAp) nucleation. Therefore, a convincing temporal and/or spatial characterization of phosphate formation in natural or synthetic samples is still lacking (e.g. 5, 8, 15, 27-28) despite the use of sophisticated time-resolved measurements and simulations performed in the last two decades, such as *in situ* X-ray absorption (XAS), *in situ* small/wide-angle X-ray scattering (SAXS/WAXS), electron transmission microscopy (Cryo-TEM or liquid-cell TEM), atomic force microscopy (liquid-cell AFM) and *ab initio* numerical simulations based on the density functional theory (e.g. 1, 12-13, 19, 25-27, 29-30). Despite all these available techniques, more knowledge is required to understand how phosphate minerals nucleate and grow from solutions and slurries. In this context, time-resolved Raman spectroscopy measurements provide invaluable information on the nucleation, transformation and growth of particles and crystals, as recently demonstrated for several carbonates (31-33) and phosphates minerals (34-37). This spectroscopy technique allows discriminating between amorphous and crystalline phases that form early during the nucleation and growth of more stable minerals.

In the present study, the nucleation of brushite and hydroxyapatite was monitored in real-time and *in situ* by using Raman spectroscopy at 25 °C. For both minerals, amorphous calcium phosphate ($Ca(HPO_4)_{1-x}(PO_4)_{(2/3)x}.nH_2O$) with different Raman signature instantaneously formed as ionic solutions were rapidly mixed under mechanical stirring. Then, the amorphous phases transformed rapidly or slowly into OCP (crystalline transient phase). Finally, OCP transformed into brushite micro-crystals or into hydroxyapatite nanocrystals depending on the experimental investigated conditions. We varied the pH, the HPO_4^{2-}/PO_4^{3-} ratio and the Ca/P ratio. The lifetime of amorphous

7

and crystalline transient phases, reaction mechanisms and kinetics of formation of brushite and hydroxyapatite were then measured. We acquired several ex-situ measurements and images of the products recovered at the end of the experiments in order to characterize the average particles size, crystal shape and mineral composition.

2. Materials and Methods

2.1. Time-lapse Raman spectroscopy

The formation of brushite and hydroxyapatite was monitored using a Raman probe (785 nm infra-red laser) immersed into a C22 Hastelloy batch reactor with internal volume of 600 ml. This experimental setup is described in a previous study (31). Raman spectra were collected with an exposure time of three or two seconds and averaged over three or two scans. The delay between successive acquisitions varied between fifteen seconds and one hour, depending on the investigated reaction. The duration of experiments was arbitrarily imposed from 2h to 24h and all collected spectra were saved on the control computer.

Selected Raman peaks (strongest peak) corresponding to identified mineral phases (see Table S1 and Table 1) were fitted by using simple or combined Gaussian models in order to calculate the peak Full Width at Half-Maximum (FWHM) and the integrated peak surface area as a function of time (Movie S1). The Raman signals were fitted using the following procedure. First, we selected a small region of the entire Raman spectrum that contained only the peaks relevant for the reaction studied. Then, the baseline was removed to correct for temporal fluctuations of the intensity of the signal. Finally, we decomposed the Raman signal into two, three, or four Gaussian curves,

8

depending on the number of species present in the system. For each species, the position of the peak was fixed and the amplitude and standard deviation of each Gaussian was fitted using a non-linear least squares method (Movies S1, S2, S3). This calculation provides the peak decomposition necessary to propose relevant reaction mechanisms and to quantify the kinetics of formation of calcium phosphates phases in aqueous solutions or slurries, including nucleation time and lifetime of minerals and aqueous species.

2.2. Brushite ($CaHPO_4.2H_2O$) from a phosphate solution

200 ml of phosphate solution (0.2M of Na_2HPO_4, pH~9.8) were firstly placed in the reactor under continuous stirring (400 rpm) at a temperature of ~25°C. Raman spectroscopy monitoring reveals a strong peak at 993 cm^{-1}, characteristics of HPO_4^{2-}, before the addition of a calcium solution (Figure S1a). Then, 200 ml of calcium solution (0.2M of $CaCl_2$, pH~6.8) were rapidly added into the system with a syringe for about one to two minutes leading to the instantaneous formation of a gel-like amorphous calcium phosphate phase with a Raman peak at 957 cm^{-1} (Figure S1b). The chemical transformation of this amorphous phase to crystalline phases was then monitored for 23h with an acquisition frequency of one Raman spectrum every fifteen seconds during the first twenty minutes and every minute or five minutes in the remaining time. The same experiment was performed in presence of 1g of citric acid ($C_6H_8O_7$), initially dissolved in the calcium solution in order to assess the effect of this acid on the kinetics and reaction mechanism. The citric acid is used here as a complexing agent that is expected to stabilize transient amorphous phosphate phases for longer durations than without acid. All chemical reactants with high purity (>99%) were provided by Sigma-Aldrich.

9

2.3. Hydroxyapatite from Na₂HPO₄-Ca(OH)₂ slurry

200 ml of deionized water (18.2 megaohm of resistivity) and 3g of $Ca(OH)_2$ (>96% of purity provided by Sigma-Aldrich) were placed in the reactor under continuous stirring (400 rpm) at a temperature of ~25°C. Direct Raman spectroscopy monitoring reveals a peak at 362 cm^{-1}, characteristics of calcium hydroxide, before the addition of a phosphate solution (Figure S2). After the addition of 200ml of a phosphate solution (0.2M of Na_2HPO_4, pH~9.8), the calcium hydroxide progressively dissolves (Figure S2) while hydroxyapatite forms under an alkaline pH higher than 12, constrained by the release of OH^- ions, as shown in the following overall reaction:

$$10Ca(OH)_2 + 6HPO_4^{2-} \Rightarrow Ca_{10}(PO_4)_6(OH)_2 + 12OH^- + 6H_2O \tag{1}$$

This overall reaction involves the formation of amorphous and crystalline transient phases that were monitored in real-time by Raman spectroscopy for 18h with an acquisition frequency of one Raman spectrum every fifteen seconds during the first twenty minutes, and every minute or five minutes in the remaining time. The same experiment was performed in presence of 1g of citric acid ($C_6H_8O_7$), initially dissolved in the calcium hydroxide slurry

2.4. Hydroxyapatite from ionic solutions

200 ml of phosphate solution (0.2M of PO_4^{3-}/HPO_4^{2-}, pH~12.4 adjusted with NaOH) were firstly placed in the reactor under continuous stirring (400 rpm) at a temperature of ~25°C. Direct Raman spectroscopy monitoring confirms the presence of peaks for HPO_4^{2-} at 992 cm^{-1} and PO_4^{3-} at 939 cm^{-1}, before the addition of a calcium solution (Figure S3a). Then, 200 ml of calcium solution

(0.33M of $CaCl_2$) were rapidly added into the system with a syringe for about 1-2 minutes. Similar to the brushite experiment, the fast mixing of these two ionic solutions led to the instantaneous formation of a gel-like phase that contained an amorphous calcium phase with a Raman peak at 951 cm^{-1} (Figure S3b). The lifetime and chemical transformation of this gel into crystalline phases were monitored in real-time for 23h with an acquisition frequency of one Raman spectrum every fifteen seconds during the first twenty minutes and every minute or five minutes in the remaining time. The overall reaction to form hydroxyapatite can be written as follows:

$$2HPO_4^{2-} + 4PO_4^{3-} + 2OH^- + 10Ca^{2+} \Rightarrow Ca_{10}(PO_4)_6(OH)_2 + 2H^+ \tag{2}$$
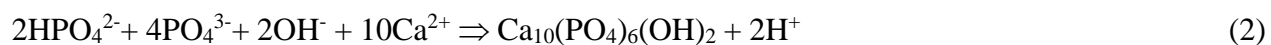
In contrast to the formation of hydroxyapatite from a calcium hydroxide slurry (reaction 1), the synthesis of hydroxyapatite using ionic solutions releases protons, which produces a decrease of pH during the experiment from ~12.4 to ~11.

In summary, three different pH regimes were investigated in this study using equimolar Ca/P ratio or hydroxyapatite stochiometric ratio (Ca/P=1.66) and two different Ca sources ($CaCl_2$ and $Ca(OH)_2$). The pH in the solutions and slurries was systematically measured at the beginning and the end of each experiment. We used a conventional pH meter (Mettler Toledo MA235). However, the in-situ pH variations during precipitation experiments were not recorded. Table 1 summarizes all experiments performed in the present study. Each experiment was repeated at least three times to verify the reproducibility of the results.

11

2.5. Ex situ characterization of precipitates

At the end of each experiment, the solid product was recovered by centrifugation and washed twice with ultrapure water and once with ethanol. Then, it was dried at 60°C for 48h. The dry solid products were stored in plastic flasks for subsequent characterization of selected samples by field emission gun scanning electron microscopy (FESEM) and powder X-ray diffraction (XRD).

For high resolution imaging, the solid products were dispersed by ultrasonic treatment in absolute ethanol for five to ten minutes. One or two droplets of the suspension were then deposited directly on an aluminum support and coated with gold and platinum. The morphology of the crystals was imaged using a Zeiss Ultra 55 field emission gun scanning electron microscope (FESEM) with a maximum spatial resolution of approximately 1nm at 15kV.

XRD analyses were performed using a Siemens D5000 diffractometer in Bragg-Brentano geometry, equipped with a theta-theta goniometer with a rotating sample holder. The XRD patterns were collected using Cu kα_1 ($\lambda_{k\alpha1}$=1.5406 Å) and kα_2 ($\lambda_{k\alpha2}$=1.5444 Å) radiations in the range 2θ = 10 - 70° with a step size of 0.04° and a counting time of six seconds per step.

3. Results and discussion

3.1 Brushite formation: Reaction mechanism and kinetics

The quick mixing of two equimolar ionic solutions, one containing HPO_4^{2-}(0.2M, pH~9.8) and the other containing Ca^{2+}(0.2M, pH~6.8), leads the instantaneous formation of an amorphous calcium phosphate (ACP: $CaHPO_4.nH_2O$) with a peak at 957 cm^{-1} (Figure S1b). This Raman signature is

12

transient with a lifetime of about two minutes. Then, ACP transforms into octo-calcium phosphate

(OCP: $Ca_8(HPO_4)_2(PO_4)_4.5H_2O$) with a peak at 962 cm^{-1}. This crystalline phase nucleates from

ACP after two minutes and its maximum Raman intensity is reached after five minutes. The OCP

is also a transient phase that progressively transforms into brushite ($CaHPO_4.2H_2O$), with a peak

at 990 cm^{-1}, after a nucleation time of 7.5 minutes. Brushite reaches a maximum Raman intensity

after 24 minutes. The progressive increase of the brushite Raman peak is proportional the decrease

of OCP Raman intensity until the total consumption of OCP. This sequence of reactions and

kinetics are summarized in Figure 1, Figure S4 and Movie S1. Based on these data, the following

reaction mechanism is proposed:

1. Instantaneous formation of ACP:

$$HPO_4^{2-} + Ca^{2+} + nH_2O \Rightarrow CaHPO_4.nH_2O \tag{3}$$

Amorphous calcium phosphate containing only HPO_4^{2-} (Ca/P =1) is assumed at this investigated

pH regime where only HPO_4^{2-} ions may exist in solution. However, the incorporation of phosphate

into the amorphous phase ($Ca(HPO_4)_{1-x}(PO_4)_{(2/3)x}.nH_2O$) and the removal of protons (H^+) at the

solid-fluid interface are not excluded.

2. Transformation of ACP into OCP via a solid-state crystallization pathway:

$$8CaHPO_4.nH_2O + 5H_2O \Rightarrow Ca_8(HPO_4)_2(PO_4)_4.5H_2O + 2H_2PO_4^- + 2H^+ + 8nH_2O \tag{4}$$
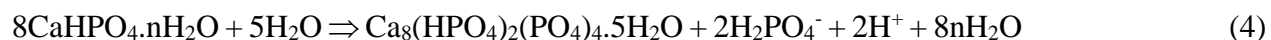
This reaction implies the protonation of residual phosphate ions as confirmed by the peaks at 880

and 1080 cm^{-1} assigned to $H_2PO_4^-$ (Figure S5 and Table S1). This means that a significant decrease

of pH (probably, pH<6.7) takes place in first minutes that favor then the OCP transformation into

13

brushite as directly monitored by Raman spectroscopy (Figure 1) and described below by reaction 5.

In addition, a solid-state crystallization is assumed because the overall transformation of ACP into OCP takes place abruptly in less than fifteen seconds, which corresponds to the time resolution in our experiments, as illustrated in Figure 1.

3. Transformation of OCP into brushite via a dissolution-recrystallization pathway:

$$Ca_8(HPO_4)_2(PO_4)_4.5H_2O + 2H_2PO_4^- + 2H^+ + 11H_2O \Rightarrow 8CaHPO_4.2H_2O \tag{5}$$
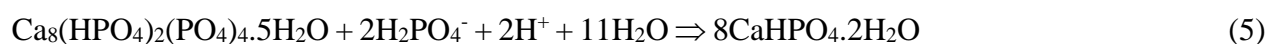
Dissolution-recrystallization pathway is here assumed because the OCP transient phase is progressively consumed by the formation and growth of brushite (Figure 1). This interpretation is supported by a temporal increase the FWHM of the main OCP Raman peak until its total consumption (Figure S6). This result can be interpreted by an average decrease of the crystals size, z, of OCP with z α 1/FWHM$_{OCP}$, due to a progressive dissolution process. Conversely, the temporal decrease of FWHM for brushite formation indicates a crystal growth process.

Ex-situ characterization of solids recovered at the end of experiments by FESEM and XRD confirmed the presence of elongated microcrystals (>20µm) of brushite (see Figure S7).

In the presence of citric acid, the reaction mechanism remains very similar because the reactions 3 to 5 occur and the only measurable difference is a very slight transformation of brushite into hydroxyapatite confirmed by XRD in the recovered solid product (experiment 2 in Table 1 and Figure S8). In presence of citric acid, the transformation kinetics, and mainly the transformation of OCP into brushite (reaction 5), are significantly retarded from 15 (Figure 1) to 400 minutes (Figure 2). Conversely, the formation of ACP (reactions 3) and the transformation of ACP into OCP

14

(reaction 4) are only slightly retarded, as displayed in Figure 2.

3.2 Hydroxyapatite formation from Ca(OH)₂ slurry: Reaction mechanism and kinetics

In this case, a phosphate ionic solution (0.2M of HPO_4^{2-}, pH~9.8) was rapidly added to a $Ca(OH)_2$ slurry (0.015g/g_{H2O}, pH~12.2). As expected, an amorphous calcium phosphate (ACP1) with a peak at 954 cm^{-1} forms instantaneously in the first fifteen seconds, and has a lifetime of less than one minute. The ACP1 rapidly transforms into another amorphous calcium phase with a peak at 943 cm^{-1} (ACP2), a transformation accompanied by a transient release of HPO_4^{2-} ions with a peak at 993 cm^{-1} (Figure 3). Based on this result, we assume that the shift of the peak position of the calcium amorphous phases is exclusively related to the HPO_4^{2-} or PO_4^{3-} structural content into the amorphous phase $(Ca(HPO_4)_{1-x}(PO_4)_{(2/3)x}.nH_2O$; with x that varies between 0 and 1). Therefore, the calcium amorphous phase can show a Raman signature with broad peaks between 943 cm^{-1} for $Ca_3(PO_4)_2.nH_2O$ (ATCP), and 957 cm^{-1} for $CaHPO_4.nH_2O$ (ACP). This result is illustrated in Figure S9, where the parameter x can be calculated by a linear interpolation of the peak position in the interval 943-957cm^{-1} (x=68.357 – (1/14)*P_{ACP}: where P_{ACP} is the position in cm^{-1} comprised between 943 and 957). Then, the ATCP slowly transforms into hydroxyapatite with a peak at 963 cm^{-1}. The OCP clearly detected in the brushite systems as a transient phase (experiments 1 and 2) is also expected to form in more alkaline systems. However, the strongest Raman peak of OCP (962 cm^{-1}) is very close to the main peak of hydroxyapatite (963 cm^{-1}). For this reason, the OCP-like layers transient phase is also considered in the deconvolution peak fitting, as illustrated in the Movie S2, and in the kinetics behavior summarized in Figure S10. Note that the OCP-like layers formation in this particular case remains speculative because we did not detect this phase in the solid product after the experiment. However, we needed this phase to fit the Raman data. Based on

15

these time-resolved Raman spectroscopy measurements, the following reaction mechanism is suggested:
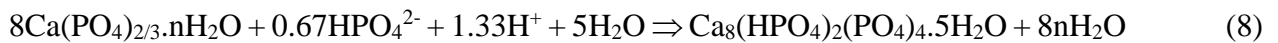
1. Instantaneous formation of ACP1:

$$HPO_4^{2-} + Ca^{2+} + nH_2O \Rightarrow Ca(HPO_4)_{0.8}(PO_4)_{0.13}.nH_2O + 0.07PO_4^{3-} + 0.2H^+ \tag{6}$$
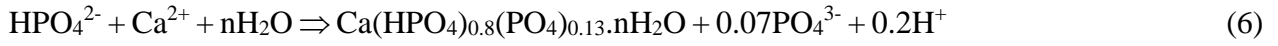
Here, we assume that the produced protons (H^+) are instantaneously neutralized by the calcium hydroxide dissolution ($Ca(OH)_2 \Rightarrow Ca^{2+} + 2OH^-$) such that a high alkaline pH (>12.2) is maintained during the experiment as expected by overall reaction 1 (see the section Materials and Methods).

2. Transformation of ACP1 into ATCP via a solid-state transformation pathway:

$$Ca(HPO_4)_{0.8}(PO_4)_{0.13}.nH_2O \Rightarrow Ca(PO_4)_{2/3}.nH_2O + 0.27HPO_4^{2-} + 0.53H^+ \tag{7}$$
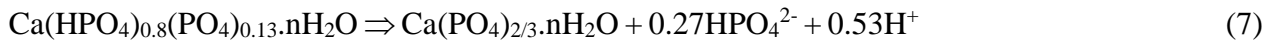
Solid-state transformation is assumed because ACP1 has a short lifetime, less than one minute, and its transformation into ATCP takes place abruptly, as shown in Figure 3. The phase $Ca(PO_4)_{2/3}.nH_2O$ is equivalent to $Ca_3(PO_4)_2.nH_2O$ reported in the literature and is constituted mainly by the so-called Posner's clusters $Ca_9(PO_4)_6$ with ~1 nm size (11). The reaction 7 implies a release of HPO_4^{2-} ions and protons (H^+) that are also detected by Raman spectroscopy (Figure 3). These ions rapidly react to form OCP as illustrated in the following reaction, and residual phosphate ions are transformed to PO_4^{3-}, the main phosphate aqueous species in high alkaline aqueous media. Residual protons (H^+) are neutralized to water ($H^+ + OH^- \Rightarrow H_2O$).

3. Transformation of ATCP to OCP-like layers:

$$8Ca(PO_4)_{2/3}.nH_2O + 0.67HPO_4^{2-} + 1.33H^+ + 5H_2O \Rightarrow Ca_8(HPO_4)_2(PO_4)_4.5H_2O + 8nH_2O \tag{8}$$
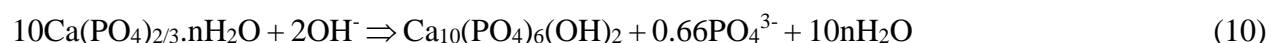
As indicated above, only OCP-like layers were suspected in the raw Raman data, but, it is necessary to improve the deconvolution fitting, particularly in the first 90 minutes (see Figure S10 and Movie

16

S2). Moreover, the ATCP phase has a long lifetime and coexists with hydroxyapatite until the end of the experiment. For this reason, two different mechanisms may occur simultaneously to form hydroxyapatite in high alkaline media.

4a. Transformation of OCP-like layers into hydroxyapatite:

$$Ca_8(HPO_4)_2(PO_4)_4.5H_2O + 2Ca^{2+} + 2OH^- \Rightarrow Ca_{10}(PO_4)_6(OH)_2 + 2H^+ + 5H_2O \tag{9}$$
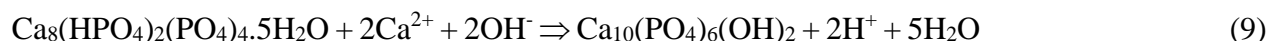
4b. Transformation of ATCP into hydroxyapatite:

$$10Ca(PO_4)_{2/3}.nH_2O + 2OH^- \Rightarrow Ca_{10}(PO_4)_6(OH)_2 + 0.66PO_4^{3-} + 10nH_2O \tag{10}$$

Both reactions (9 and 10) participate to the formation of hydroxyapatite, as shown by the temporal behavior of the Raman intensity of selected peaks (Figure 4) and the integrated peak surface areas of concerned phases (Figure S10 and Movie S2). However, the low temporal variation of the FWHM parameter (Figure S11) does not allow to conclude if the reactions takes place via a dissolution-recrystallization pathway, as clearly deduced for brushite system. In this case, partial dissolution, i.e. conserving $Ca_9(PO_4)_6$ clusters of ~1 nm size as building primary units, combined with self-assembly aggregation could operate to form hydroxyapatite, as suggested in previous studies (11-12, 14, 16, 18). Unfortunately, Raman dynamic in situ monitoring cannot provide clear or complementary information on this specific important interfacial process.

Ex-situ characterization of solids recovered after the experiments by FESEM and XRD confirm the presence of acicular nanocrystals of hydroxyapatite, with size <100nm, and, probably, some residual amorphous calcium phosphate, as attested by the presence of very fine particles with size < 20nm (Figure S12).

Concerning the effect of citric acid, Raman data reveal that the reaction mechanism remains very similar because the reactions 6 to 10 can be confirmed. The main difference concerns reaction 6

17

where the transient amorphous calcium carbonate (ACP1) has a Raman signature at 957cm^{-1}, and therefore contains only HPO$_4^{2-}$ in its structure (CaHPO$_4$.nH$_2$O), as illustrated in Figure S9. The other difference is that the transformation kinetics of transient phases into hydroxyapatite, including the nucleation time (reactions 8-10) is significantly retarded, as illustrated in Figure 5. Conversely, the formation of ACP1 (reaction 6) and the transformation of ACP1 to ATCP (reaction 7) are slightly retarded only.

3.3 Hydroxyapatite formation from mixture of ionic solutions: Reaction mechanism and kinetics

The quick mixing of two ionic solutions with hydroxyapatite stochiometric ratio, Ca/P=1.66, one containing 0.2M of PO$_4^{3-}$/HPO$_4^{2-}$ (pH~12.4 adjusted with NaOH) and the other containing Ca^{2+}(0.33M, pH~6.8), leads to the instantaneous formation of amorphous calcium phosphate (ACP: Ca(HPO$_4$)$_{1-x}$(PO$_4$)$_{(2/3)x}$.nH$_2$O; x=0.43) with a peak at 951cm^{-1} (Figure 6). This Raman signature is transient with a short lifetime of three to four minutes. The total lifetime of ACP is about 30 minutes, and the position of its Raman peak varies from 951 cm^{-1} (x=0.43) to 954 cm^{-1} (x=0.21) prior to its transformation into OCP. Then, OCP is transformed into hydroxyapatite with a nucleation time of 36 minutes (Figure 6). This result is supported by the deconvolution fitting of selected Raman peaks (Figure S13 and Movie S3). The formation of OCP-like layers in this case remains speculative, but in agreement with literature (5, 27, 28). Based on these time-resolved Raman spectroscopy measurements, the following reaction mechanism steps are proposed:
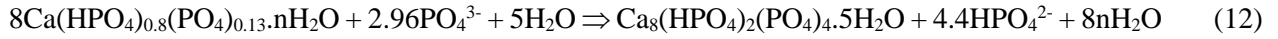
1. Instantaneous formation of ACP:

$$(1-x)HPO_4^{2-} + (2/3)xPO_4^{3-} + Ca^{2+} + nH_2O \Rightarrow Ca(HPO_4)_{1-x}(PO_4)_{(2/3)x}.nH_2O \tag{11}$$

Here, x varies between 0.43 and 0.21, i.e. the ACP is structurally enriched with HPO$_4^{2-}$ as a function of time prior to its transformation into OCP-like layers. Clusters aggregation process combined

18

with partial dissolution could be the responsible to this variation of phosphate content into ACP.

2. Transformation of ACP into OCP-like layers:

$$8Ca(HPO_4)_{0.8}(PO_4)_{0.13}.nH_2O + 2.96PO_4^{3-} + 5H_2O \Rightarrow Ca_8(HPO_4)_2(PO_4)_4.5H_2O + 4.4HPO_4^{2-} + 8nH_2O \qquad (12)$$

A solid-state transformation is proposed because the transformation of ACP into OCP-like layers takes place over a short duration, in less than two minutes, and the position of the Raman peak shifts rapidly from 954 cm^{-1} to 959 cm^{-1} (Figure 6).

3. Transformation of OCP-like layers into hydroxyapatite:

$$Ca_8(HPO_4)_2(PO_4)_4.5H_2O + 2Ca^{2+} + 2OH^- \Rightarrow Ca_{10}(PO_4)_6(OH)_2 + 2H^+ + 5H_2O \qquad (13)$$
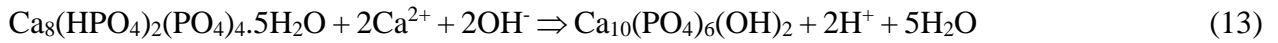
As explained above, the partial dissolution of OCP-like layers and ACP conserves $Ca_9(PO_4)_6$ clusters of ~1 nm size as primary building unit (11, 16). These clusters can aggregate to form hydroxyapatite as described in the literature (11-12, 14, 16, 18). This interpretation is supported by the slight progressive shift of the position of the Raman peak from 960 to 962cm^{-1} and the slight decrease of FWHM of hydroxyapatite (Figure S14).

4. Concluding remarks

Time-resolved Raman measurements reveal that amorphous calcium phosphate $(Ca(HPO_4)_{1-x}(PO_4)_{(2/3)x}.nH_2O)$ has specific Raman signature comprised between 943 cm^{-1} for ATCP $(Ca_3(PO_4)_2.nH_2O, x=1)$ and 957 cm^{-1} for ACP $(CaHPO_4.nH_2O, x=0)$, as shown in the Figures 1, 3, 6 and S9. This specific Raman signature does not overlap with the strongest Raman peaks of crystalline calcium phosphates phases formed at ambient temperature (OCP at 960-962 cm^{-1}, brushite at 990 cm^{-1} and hydroxyapatite at 962-963 cm^{-1}) and aqueous species ($H_2PO_4^-$ at 880 cm^{-1} and 1080 cm^{-1}, HPO_4^{2-} at 992-993 cm^{-1}, and PO_4^{3-} at 939 cm^{-1}). Based on these spectral Raman
19

signatures monitored in real-time and under *in situ* conditions, we demonstrate that the ACP that contains only HPO_4^{2-} in its structure ($CaHPO_4.nH_2O$, $x=0$) has a short lifetime (<5min) in solution (experiments 1-2 in Table 1, Figures 1-2). Conversely, the ATCP that contains only PO_4^{3-} in its structure ($Ca(PO_4)_{(2/3)}.nH_2O$ or $Ca_3(PO_4)_2.nH_2O$, $x=1$) has a much longer lifetime (>24h) in solution (experiments 3-4 in Table 1, Figure 5). These results are supported by experiment 5 (Table 1), where the ACP contains initially both PO_4^{3-} and HPO_4^{2-} in its structure with $x=0.4$. This phosphate composition in ACP varies with time until $x=0.2$ prior to its crystallization into a more stable phase. In this case, an intermediate lifetime of ~35 minutes is measured (Figure 6). In addition to these fundamental insights, the reaction mechanism steps and kinetics during crystallization of brushite and hydroxyapatite can be determined under specific experimental conditions. For example, brushite ($CaHPO_4.2H_2O$) forms when the pH is < 9.8; amorphous calcium phosphate (ACP: $CaHPO_4.nH_2O$) with short lifetime (<2 minutes) and octocalcium phosphate (OCP: $Ca_8(HPO_4)_2(PO_4)_4.5H_2O$) are the main transient phases prior to the nucleation of brushite that occurs after ~8 minutes (see reactions 3-5). When pH is > 11, the hydroxyapatite ($Ca_{10}(PO_4)_6(OH)_2$) nucleates rapidly, after about 35 minutes, depending on the experimental conditions. Herein, amorphous calcium phosphate with different chemical compositions (ATCP: $Ca(HPO_4)_{1-x}(PO_4)_{(2/3)x}.nH_2O$; x from 0.2 to 1) and with different lifetimes can form and then transform into OCP-like layers. Then, the OCP transient phase transforms into hydroxyapatite. The ATCP phase can also transform directly into hydroxyapatite when pH is > 12.2, without forming OCP as an intermediate phase (see reactions 6-10 and/or 11-13). In conclusion, the present study reports fundamental insights on the formation of amorphous calcium phosphate phases and their transformation into brushite micro-crystals or hydroxyapatite nanocrystals under abiotic conditions, relevant to technological applications and/or natural settings.

20

The early formation of amorphous phases and their transformation into transient or stables crystalline phases is now considered to be a generalized reaction pathway during the formation of calcium carbonate and phosphate minerals and/or biominerals in aqueous systems. This crystallization pathway agrees with Ostwald's rule, but transient phases are not necessary polymorphs; in fact, they can have different chemical compositions and different particle sizes. Moreover, thermodynamic and kinetic arguments should be considered in the crystallization tendency (e.g. 38, this study). In this way, multi-steps nucleation events may exist and combine various reaction mechanisms at the solid-fluid interfaces. Thus, solid-state transition, dissolution-recrystallization, self-assembly aggregation and partial dissolution-aggregation may operate together during nucleation and growth processes (e.g. 31-33 and the present study). In this case, the classical nucleation theory (CNT), the most common theoretical formalism to quantify nucleation and growth rates (including variation of particles size distribution) cannot successfully be applied in its original formalism as proposed in the last three decades by various research groups (e.g. 39-42). These groups have proposed an alternative descriptive approach called non-classical nucleation and crystallization pathways (including pre-nucleation clusters). However, in the absence of a theoretical quantitative formalism to describe the so-called nonclassical nucleation, the improved and/or adapted classical nucleation theory remains the best tool to simulate non-classical nucleation of crystals and/or particles (e.g. 12, 43-45).

Supporting Information Available

Table S1 and Figures S1−S14 as described in the text (PDF). Time evolution of the peaks of the main mineral phases during experiments 1, 3 and 5 (AVI)

Acknowledgements

23

References

(1) Wang, X.; Jie Yang, J.; Andrei, C. M.; Soleymani, L.; Grandfield, K. Biomineralization of calcium phosphate revealed by in situ liquid-phase electron microscopy. *Comm. Chem.* **2018***, 1:80*

(2) Niu, X.; Liu, Z.; Tian, F.; Chen, S.; Lei, L.; Jiang, T.; Feng, Q.; Fan, Y. Sustained delivery of calcium and orthophosphate ions from amorphous calcium phosphate and poly(L-lactic acid)-based electrospinning nanofibrous scaffold. *Sci. Rep.* **2017***, 7:45655*

(3) de Aza, P. N. ; Santos, C. ; Pazo, A. ; de Aza, S. ; Cusco, R. ; Artús L. Vibrational Properties of Calcium Phosphate Compounds. 1. Raman Spectrum of β-Tricalcium Phosphate. *Chem. Mater.* **1997,** *9,* 912-915.

(4) Combes, C.; Rey, C. Amorphous calcium phosphates: Synthesis, properties and uses in biomaterials. *Acta Biomater.* **2010***, 6,* 3362-3378.

(5) Eliaz, N.; Metoki, N. Calcium Phosphate Bioceramics: A Review of Their History, Structure, Properties, Coating Technologies and Biomedical Applications. *Materials* **2017***, 10*, 334.

(6) Bohner, B.; Bánsági Jr., T.; Tóth, A.; Horváth, D.; Taylor, A. F. Periodic Nucleation of Calcium Phosphate in a Stirred Biocatalytic Reaction. *Angew. Chem. Int. Ed.* **2020***, 59*, 2823–2828.

(7) Cross, K. J.; Huq, N. L.; Reynolds, E. C. Casein Phosphopeptide−Amorphous Calcium Phosphate Nanocomplexes: A Structural Model. *Biochem.* **2016***, 55*, 4316−4325.

(8) Lotsari, A.; Rajasekharan, A. K.; Halvarsson, M.; Andersson, M. Transformation of amorphous calcium phosphate to bone-like apatite. *Nature Comm.* **2018***, 9:4170*

(9) Tsujia, T.; Onuma, K.; Yamamoto, A.; Iijima, M.; Shiba, K. Direct transformation from amorphous to crystalline calcium phosphate facilitated by motif-programmed artificial proteins. *PNAS* **2008***, 105*, 16866–16870.

(10) Zhang, Y. Y.; Wong, H. M.; McGrath, C. P. J.; Li, Q. L. *In vitro* and *in vivo* evaluation of electrophoresis-aided casein phosphopeptide-amorphous calcium phosphate remineralization system on pH-cycling and acid-etching demineralised enamel. *Sci. Rep.* **2018** *8:8904*

(11) Posner, A. S.; Betts, F. Synthetic Amorphous Calcium Phosphate and Its Relation to Bone Mineral Structure. *Acc. Chem. Res.* **1975***, 8,* 273–281.

(12) Habraken *et al.* Ion-association complexes unite classical and non-classical theories for the biomimetic nucleation of calcium phosphate. *Nature Comm.* **2013***, 4:1507*

(13) Lu, B. Q.; Garcia, N. A.; Chevrier, D. M.; Zhang, P. ; Raiteri, P.; Gale, J. D.; Gebauer, D. Short-Range Structure of Amorphous Calcium Hydrogen Phosphate. *Cryst. Growth Des.* **2019***, 19*, 3030−3038.

(14) Tao, J.; Pan, H.; Wang, J.; Wu, J.; Wang, B.; Xu, X.; Tang, R. Evolution of Amorphous Calcium Phosphate to Hydroxyapatite Probed by Gold Nanoparticles. *J. Phys. Chem. C* **2008***, 112,* 14929–14933.

25

(15) Ucar, S.; Bjørnøy, S. H.; Bassett, D. C.; Strand, B. L.; Sikorski, P.; Andreassen, J.-P. Formation of Hydroxyapatite via Transformation of Amorphous Calcium Phosphate in the Presence of Alginate Additives. *Cryst. Growth Des.* **2019***, 19*, 7077−7087.

(16) Boskey, A. L.; Posner, A. S. Conversion of Amorphous Calcium Phosphate to Microcrystalline Hydroxyapatite. A pH-Dependent, Solution-Mediated, Solid-Solid Conversion. *J. Phys. Chem.* **1973***, 112,* 14929–14933.

(17) Ibsen, C. J. S.; Leemreize, H.; Mikladal, B. F.; Skovgaard, J.; Bremholm, M.; Eltzholtz, J. R.; Iversen, B. B.; Birkedal, H. Alkali Counterions Impact Crystallization Kinetics of Apatite Nanocrystals from Amorphous Calcium Phosphate in Water at High pH. *Cryst. Growth Des.* **2018***, 18*, 6723−6728.

(18) Jiang, S.; Jin, W.; Wang, Y.-N.; Pan, H.; Sun, Z.; Tang, R. Effect of the aggregation state of amorphous calcium phosphate on hydroxyapatite nucleation kinetics. *RSC Adv.,* **2017***, 7,* 25497–25503.

(19) Kim, D.; Lee, B.; Thomopoulos, S. Jun, Y.-S. The role of confined collagen geometry in decreasing nucleation energy barriers to intrafibrillar mineralization. *Nature Comm.* **2018***, 9:962*

(20) Walton, A. G.; Bodin, A. G.; Furedi, W. J.; Schwartz, A. Nucleation of calcium phosphate from solution. *Canadian J. Chem.* **1967***, 45*, 2695-2701.

(21) Terraschke, H.; Rothe, M.; Tsirigoni, A.-M.; Lindenberg, P.; Ruiz Arana, L.; Heidenreich, N.; Bertram, F.; Etter M. In situ luminescence analysis: a new light on monitoring calcium phosphate phase transitions. *Inorg. Chem. Front.,* **2017***, 4*, 1157–1165.

(22) Cadez, V. Erceg, I.; Selmani, A.; Jurašin, D. D., Šegota, S.; Lyons, D. M.; Kralj, D.; Sikiric, M. D. Amorphous Calcium Phosphate Formation and Aggregation Process Revealed by Light Scattering Techniques. *Crystals* **2018***, 8, 254*

(23) Vecstaudza, J.; Gasik, M.; Locs, J. Amorphous calcium phosphate materials: Formation, structure and thermal behavior. *J. Eur. Ceram. Soc.* **2019***, 39,* 1642–1649.

(24) Wang, C.-G.; Liao, J.-W.; Gou, B.-D.; Huang, J.; Tang, R.-K.; Tao, J.-H.; Zhang, T.-L.; Wang, K. Crystallization at Multiple Sites inside Particles of Amorphous Calcium Phosphate. *Cryst. Growth Des.* **2009***, 9,* 2620-2626.

(25) Zhang, Q.; Jiang, Y.; Gou, B.-D.; Huang, J.; Gao, Y.-X.; Zhao, J.-T.; Zheng, L.; Zhao, Y.-D.; Zhang, T.-L.; Wang, K. In Situ Detection of Calcium Phosphate Clusters in Solution and Wet Amorphous Phase by Synchrotron X-ray Absorption Near-Edge Spectroscopy at Calcium K-Edge. *Cryst. Growth Des.* **2015***, 15*, 2204−2210.

(26) Uskoković, V. Disordering the Disorder as the Route to a Higher Order: Incoherent Crystallization of Calcium Phosphate through Amorphous Precursors. *Cryst. Growth Des.* **2019***, 19,* 4340−4357.

(27) Simon, P.; Grüner, D.; Worch, H.; Pompe, W.; Lichte, H.; El Khassawna, T.; Heiss C.; Wenisch, S.; Kniep, R. First evidence of octacalcium phosphate@osteocalcin nanocomplex as skeletal bone component directing collagen triple–helix nanofibril mineralization. *Sci. Rep.* **2018** *8:13696*

27

(28) Crane, N. J.; Popescu, V.; Morris, M. D.; Steenhuis, P.; Ignelzi Jr., M. A. Raman spectroscopic evidence for octacalcium phosphate and other transient mineral species deposited during intramembranous mineralization. *Bone* **2006***, 39*, 434–442.

(29) Michael W. Swift, M. W.; Chris G. Van de Walle, C. G.; Fisher, M. P. A. Posner molecules: from atomic structure to nuclear spins. *Phys. Chem. Chem. Phys.,* **2018**, *20*, 12373-12380.

(30) Zeng, C.; Vitale-Sullivan, C.; Ma, X. In Situ Atomic Force Microscopy Studies on Nucleation and Self-Assembly of Biogenic and Bio-Inspired Materials. *Minerals* **2017***, 7, 158*; doi:10.3390/min7090158.

(31) Montes-Hernandez, G.; Renard, F. Time-Resolved in Situ Raman Spectroscopy of the Nucleation and Growth of Siderite, Magnesite, and Calcite and Their Precursors. *Cryst. Growth Des.* **2016***, 16*, 7218-7230.

(32) Montes-Hernandez, G.; Bah, M. ; Renard, F. Mechanism of formation of engineered magnesite: A useful mineral to mitigate CO_2 industrial emissions. *J. CO_2 Util.* **2020***, 35,* 272–276.

(33) Montes-Hernandez, G.; Renard, F.; Auzende, A.-L.; Findling, N. Amorphous calcium-magnesium carbonate (ACMC) accelerates dolomitization at room temperature under abiotic conditions. *Cryst. Growth Des.* **2020***, 20,* 1434-1441.

(34) Kazanci, M.; Fratzl, P.; Klaushofer, K.; Paschalis, E. P. Complementary Information on In Vitro Conversion of Amorphous (Precursor) Calcium Phosphate to Hydroxyapatite from Raman Microspectroscopy and Wide-Angle X-Ray Scattering. *Calcif. Tissue Int.* **2006***, 79*, 354-359.

(35) Stammeiera, J. A.; Purgstaller, B.; Hippler, D.; Mavromatisa, V.; Dietzel, M. In situ Raman spectroscopy of amorphous calcium phosphate to crystalline hydroxyapatite transformation. *MethodsX* **2018***, 5,* 1241–1250.

(36) Han, B., Louhi-Kultanen, M. Real-Time Raman Monitoring of Calcium Phosphate Precipitation in a Semi-Batch Stirred Crystallizer. *Cryst. Growth Des.* **2018***, 18*, 1622−1628.

(37) Yu, M., Wang, L., Zhang, W., Ganss, B. An Evolutionarily Conserved Subdomain in Amelotin Promotes Amorphous Calcium Phosphate-to-Hydroxyapatite Phase Transition. *Cryst. Growth Des.* **2019***, 19*, 2104−2113.

(38) Van Kemenade, M. J. J. M., De Bruyn, P. L. A Kinetic Study of Precipitation from Supersaturated Calcium Phosphate Solutions. *J. Colloid Interface Sci.* **1987***, 118*, 564-585

(39) Gebauer, D.; Völkel, A.; Cölfen, H. Stable prenucleation calcium carbonate clusters. *Science* **2008**, *322*, 1819-1822.

(40) Gebauer, D.; Kellermeier, M.; Gale, J. D.; Bergstrom, L.; Colfen, H. Pre-nucleation clusters as solute precursors in crystallization. *Chem. Soc. Rev.,* **2014***, 43*, 2348-2371.

(41) Wang, T.; Cölfen, H.; Antonietti, M. Nonclassical crystallization: Mesocrystals and morphology change of CaCO3 crystals in the presence of a polyelectrolyte additive. *J. Am. Chem. Soc.* **2005***, 127*, 3246-3247.

(42) Demichelis, R.; Raiteri, P.; Gale, J. D.; Quigley, D.; Gebauer, D. Stable prenucleation mineral clusters are liquid-like ionic polymers. *Nature Comms.* **2011**, doi: 10/1038/ncomms1604.

29

(43) Hamm, L. M.; Giuffre, A. J.; Han, N.; Tao, J.; Wang, D.; De Yoreo, J. J.; Dove, P. M. Reconciling disparate views of template-directed nucleation through measurement of calcite nucleation kinetics and binding energies. *PNAS* **2014** doi: 10.1073/pnas.1312369111.

(44) Hu *et al.* The thermodynamics of calcite nucleation at organic interfaces: Classical vs. non-classical pathways. *Faraday Discuss.* **2012***, 159*, 509-523.

(45) Fritz, B.; Clément, A.; Montes-Hernandez, G.; Noguera, C. Calcite formation by hydrothermal carbonation of portlandite: complementary insights from experiment and simulation. *CrystEngComm* **2013***, 15,* 3392-3401.

Table 1. List of dynamic *in situ* Raman spectroscopy experiments performed to study the nucleation of brushite and hydroxyapatite. Experiments were performed under three different pH regimes, equimolar Ca/P ratio or hydroxyapatite stochiometric ratio (Ca/P=1.66), and two different calcium sources ($CaCl_2$ and $Ca(OH)_2$).

Expt.	Temp. (°C)	pH regime	Expt. duration (h)	Citric Acid	Transient phase(s) and principle Raman peak	Final mineral phase(s) and principle Raman peak
1	25	from 9.8-to-6.8	23	none	ACP at 957cm^{-1}	Brushite at 990cm^{-1}
					OCP at 962cm^{-1}	
2	25	from 9.8-to-6.8	18	yes	ACP at 955cm^{-1}	Brushite at 990cm^{-1}
					OCP at 962cm^{-1}	Hydroxyapatite at 963cm^{-1} (minor proportion)
3	24	pH>12.2	19	none	ACP at 954cm^{-1}	Hydroxyapatite at 963cm^{-1}
					ATCP at 943cm^{-1}	ATCP and OCP (minor proportions)
					OCP at 961cm^{-1}	
4	25	pH>12.2	20	yes	ACP at 956cm^{-1}	Hydroxyapatite at 963cm^{-1}
					ATCP at 943cm^{-1}	ATCP (significant proportion)
					OCP at 961cm^{-1}	
						OCP (minor proportion)
5	24	from 12.4 to 11	2	none	ACP1 at 951cm^{-1}	Hydroxyapatite at 962cm^{-1}
					ACP2 at 954cm^{-1}	
					OCP at 959cm^{-1}	
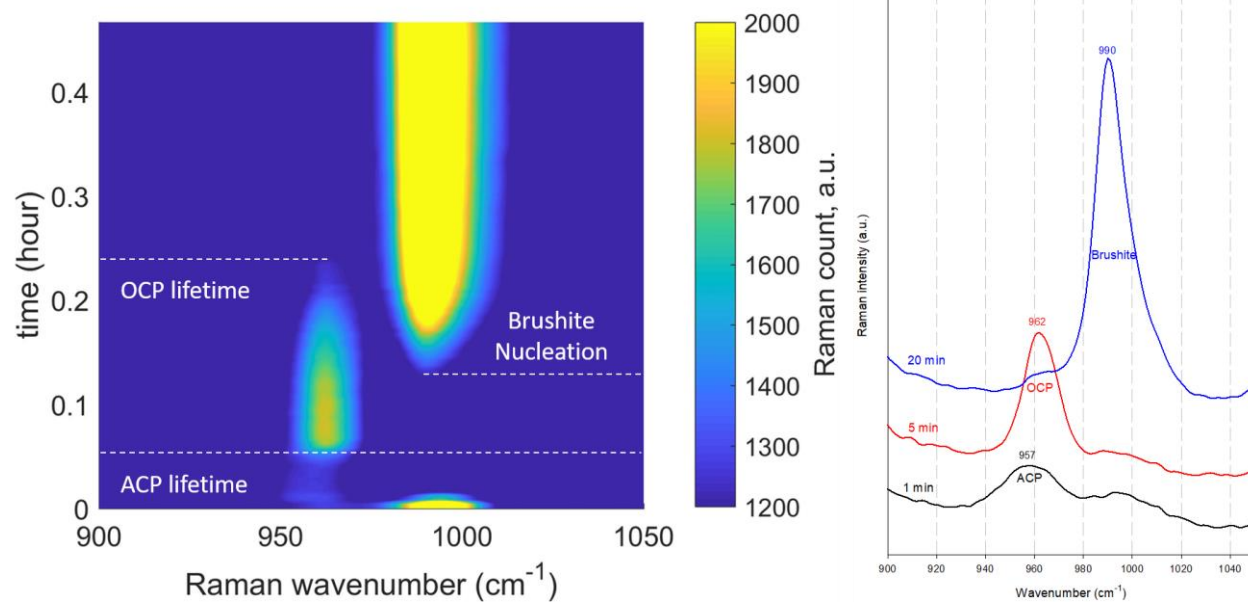
Figure 1. (left) Time-lapse Raman spectroscopy monitoring of the formation of brushite in experiment 1 (Table 1). (right) Main peaks of transient phases (ACP and OCP) and brushite, the most stable phosphate phase under the investigated conditions.
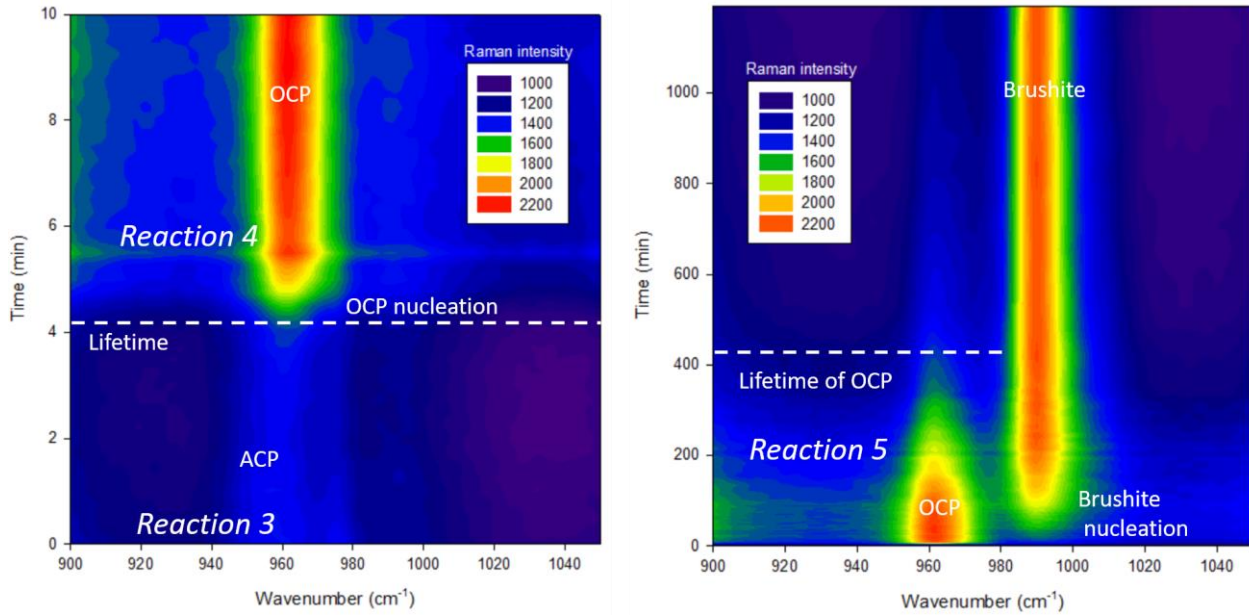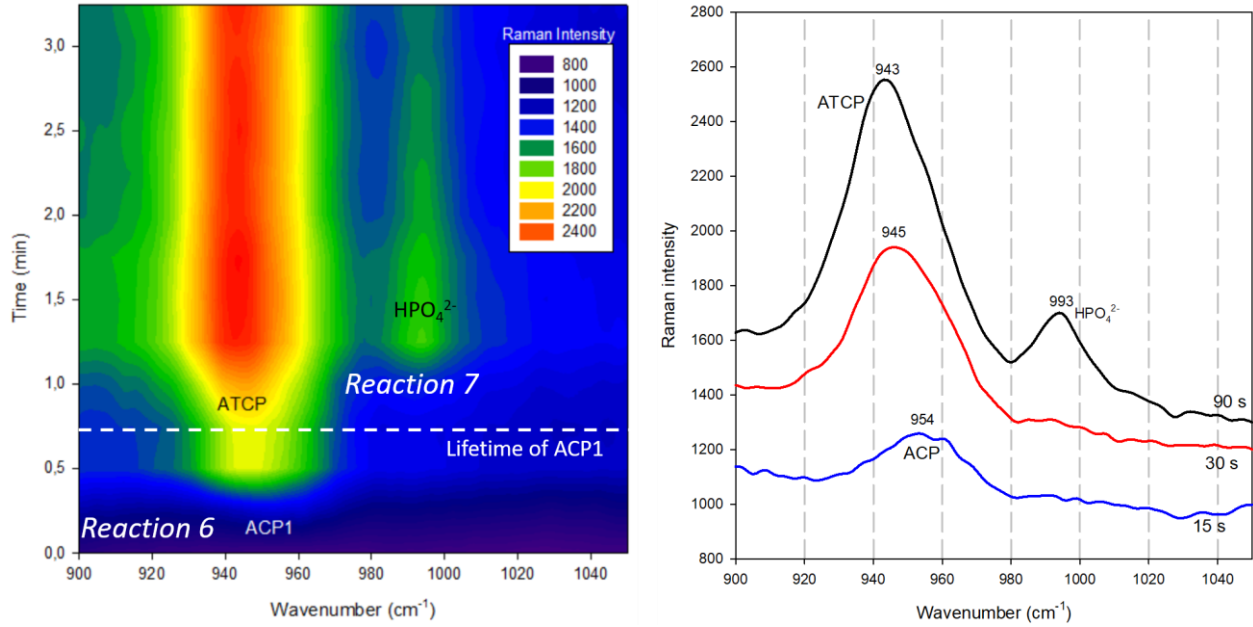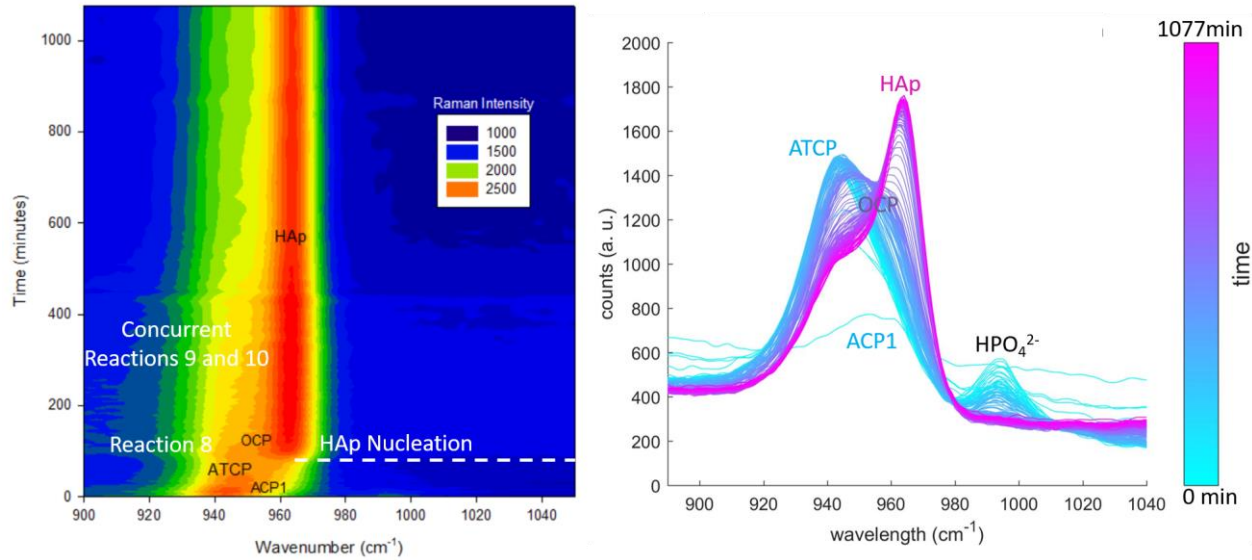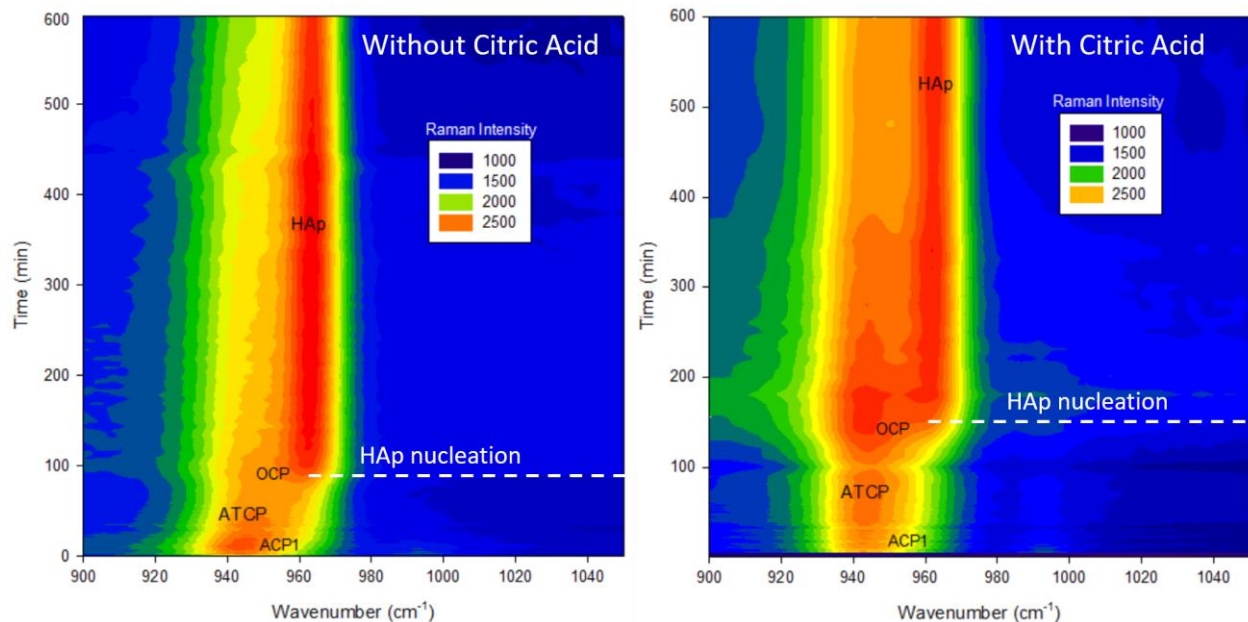
Figure 2. Time-lapse Raman spectroscopy monitoring of the formation of brushite in experiment 2 (Table 1). (left) Raw data Raman spectra between 0 and 10 minutes showing the formation of ACP (reaction 3 in the text) and the nucleation time of OCP (reaction 4 in the text). (right) Raw data Raman spectra from 0 to 1200 minutes showing the transformation of OCP into brushite (reaction 5 in the text).
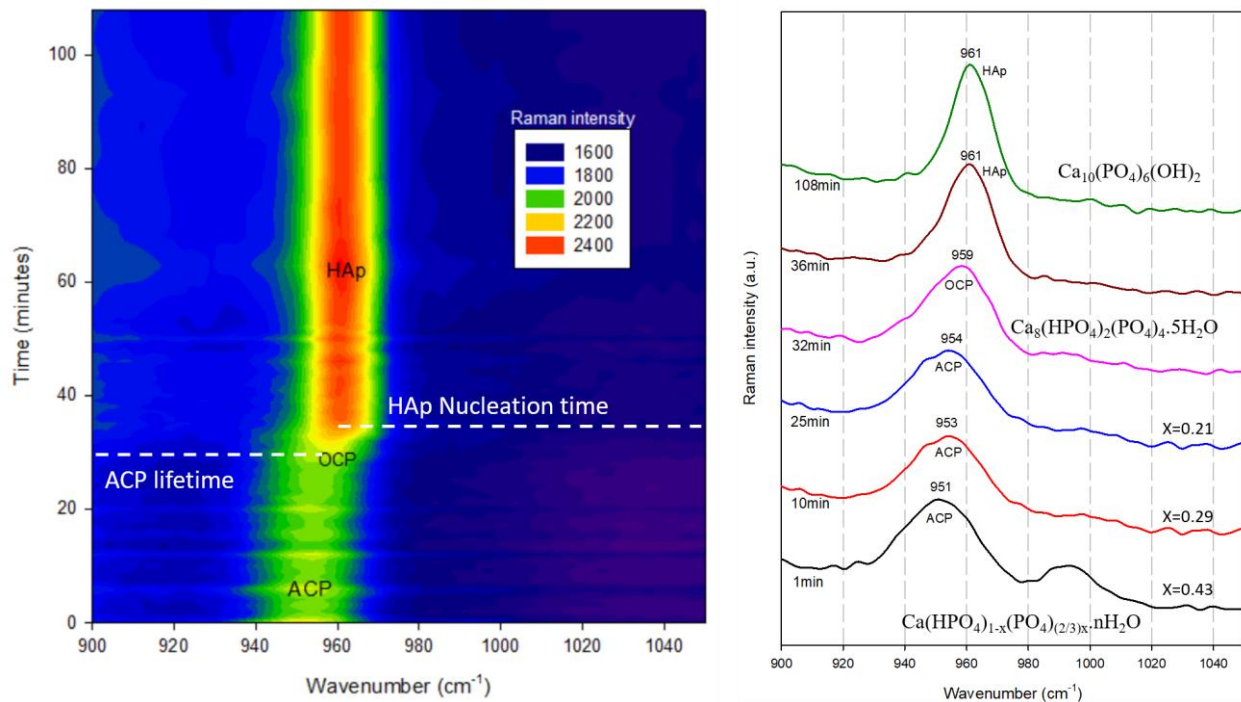
Figure 3. Time-lapse Raman spectroscopy monitoring of the formation of hydroxyapatite (HAp) in experiment 3 (Table 1). (left) Raw data Raman spectra between 0 and 3 minutes indicating the formation of ACP1 (reaction 6 in the text) and the transformation of ACP1 intoATCP (reaction 7 in the text). (right) Three raw data Raman spectra at 15, 30 and 90s showing a fast shift of the position of the Raman peak of amorphous phases from 954 to 943cm^{-1}.

Figure 4. Time-lapse Raman spectroscopy monitoring of the formation of hydroxyapatite (HAp) in experiment 3 (Table 1). (left) Raw data Raman spectra between 0 and 1077 minutes showing the transformation of ATCP into OCP (reaction 8 in the text) and the synchronous transformations of OCP into hydroxyapatite (reaction 9 in the text) and ATCP into hydroxyapatite (reaction 10 in the text). (right) Time-lapse evolution of the main peaks used for deconvolution fitting.

Figure 5. Time-lapse Raman spectroscopy monitoring of the formation of hydroxyapatite (HAp) in experiments 3 and 4 (Table 1). (left) Raw data Raman spectra between 0 and 600 minutes show the main transient calcium phosphate phases detected during hydroxyapatite formation in experiment 3. The reaction mechanism is summarized by reactions 6 to 10 in the text. (right) Raw data Raman spectra between 0 and 600 minutes showing the main transient calcium phosphate phases detected during hydroxyapatite formation in experiment 4 in presence of citric acid. The reaction mechanism is very similar than without citric acid; however, a significant retarding effect is measured as indicated by the difference of hydroxyapatite nucleation time with and without citric acid.

36

Figure 6. Time-lapse Raman spectroscopy monitoring of the formation of hydroxyapatite (HAp) in experiment 5 (Table 1). (left) Raw data Raman spectra between 0 and 108 minutes indicating the lifetime of ACP and nucleation time of hydroxyapatite. (right) Six raw data Raman spectra at 1, 10, 25, 32, 36 and 108 minutes showing the signatures of ACP, OCP and hydroxyapatite. As presented in Figure S9, phosphate content, x, was calculated using a linear interpolation ($x = 68.357 - (1/14) \cdot P_{ACP}$: where P_{ACP} is the position of the Raman peak in cm^{-1} comprised between 943 and 957).

Supporting Information for

Nucleation of brushite and hydroxyapatite from amorphous calcium phosphate phases revealed by dynamic *in situ* Raman spectroscopy

German Montes-Hernandez[a] * and François Renard[a, b]

[a] Univ. Grenoble Alpes, Univ. Savoie Mont Blanc, CNRS, IRD, IFSTTAR, ISTerre, 38000

Grenoble, France

[b] The Njord Centre, Department of Geosciences, University of Oslo, box 1048 Blindern, 0316

Oslo, Norway

*Corresponding author: G. Montes-Hernandez

E-mail address: german.montes-hernandez@univ-grenoble-alpes.fr

38

Table S1. Summary of identified calcium phosphates (solids and ions) peaks in time-resolved Raman spectroscopy measurements. These identifications are supported by studies that used ex-situ Raman spectroscopy and/or time-resolved Raman spectroscopy.

Solid phase/ aqueous specie	Formula	The most strong band in Raman (cm⁻¹)	Ref.
ACP	$CaHPO_4.nH_2O$	957	This study
		950-955	Kazanci et al. (2006) (ref. 34)
ATCP	$Ca_3(PO_4)_2.nH_2O$	943	This study
.		949-950	Stammeier et al., 2018 (ref 35)
		945-953	Yu et al., (2019) (ref. 37)
OCP	$Ca_8(HPO_4)_2(PO_4)_4.5H_2O$	959-962	This study
		955-960	Kazanci et al. (2006) (ref. 34)
		955-957	Yu et al., (2019) (ref. 37)
Brushite	$CaHPO_4.2H_2O$	990	This study
		986	Han and Louhi-Kultanen, 2018 (ref. 36)
HAp	$Ca_{10}(PO_4)_6(OH)_2$	962-963	This study
		960	Kazanci et al. (2006) (ref. 34)
		959-960	Stammeier et al., 2018 (ref 35)
Hydrogen phosphate ion	HPO_4^{2-}	992-993	This study
		990	Han and Louhi-Kultanen, 2018 (ref. 36)
Phosphate ion	PO_4^{3-}	939	This study
		936	Fontana et al., 2013
Dihydrogen phosphate ion	$H_2PO_4^-$	1080	This study
		1077	Han and Louhi-Kultanen, 2018 (ref. 36)
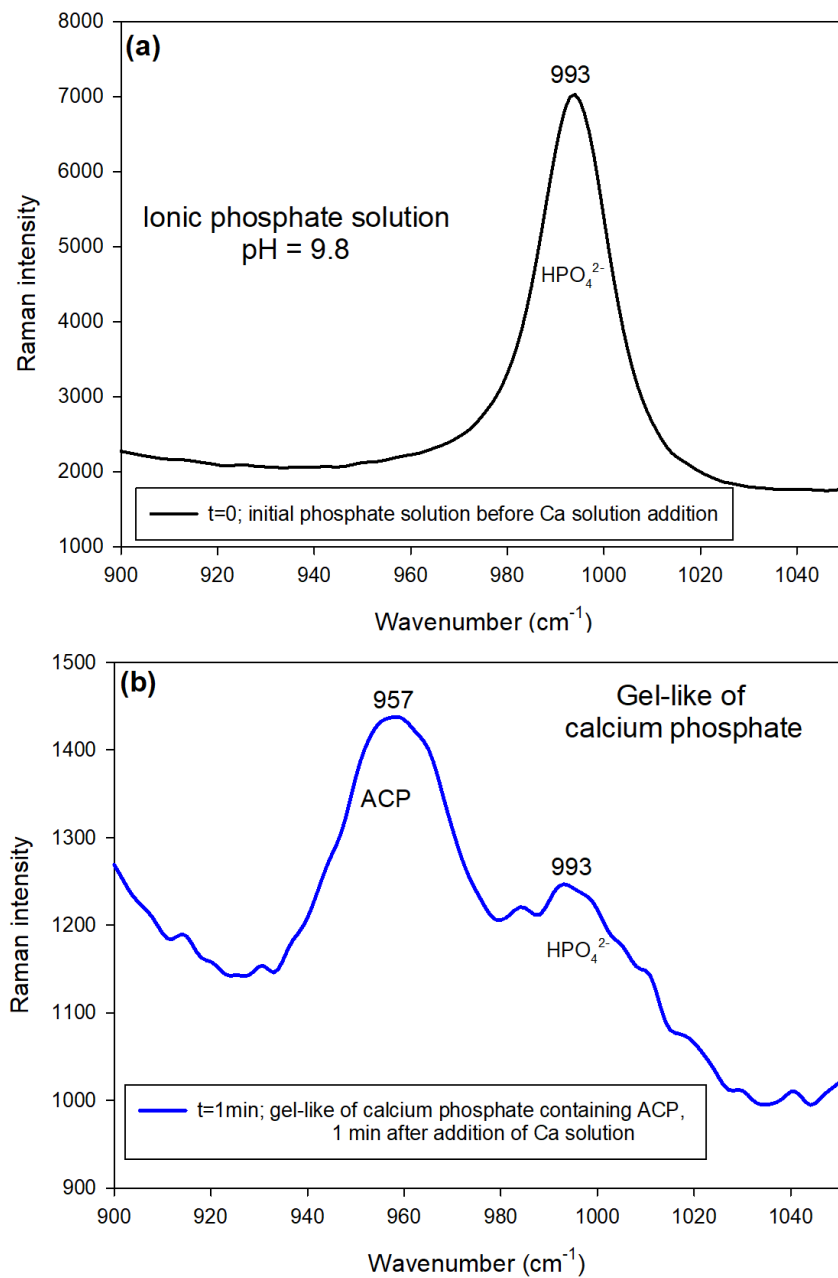
Figure S1: (a) Characterization of the initial phosphate solution by Raman spectroscopy (experiment 1). (b) *In situ* Raman spectrum of the gel-like phase formed after one minute after adding a calcium solution. The gel contains ACP and residual aqueous Ca-phosphate species (experiment 1).
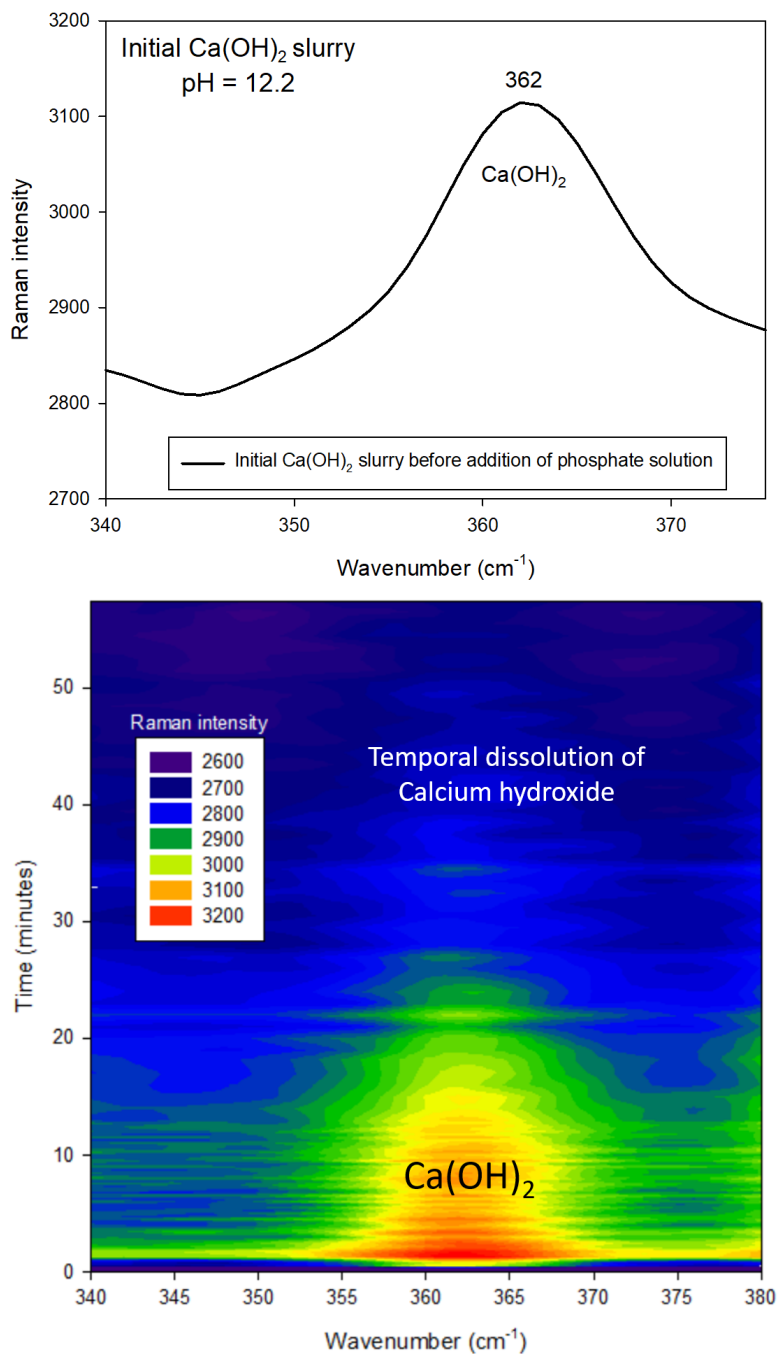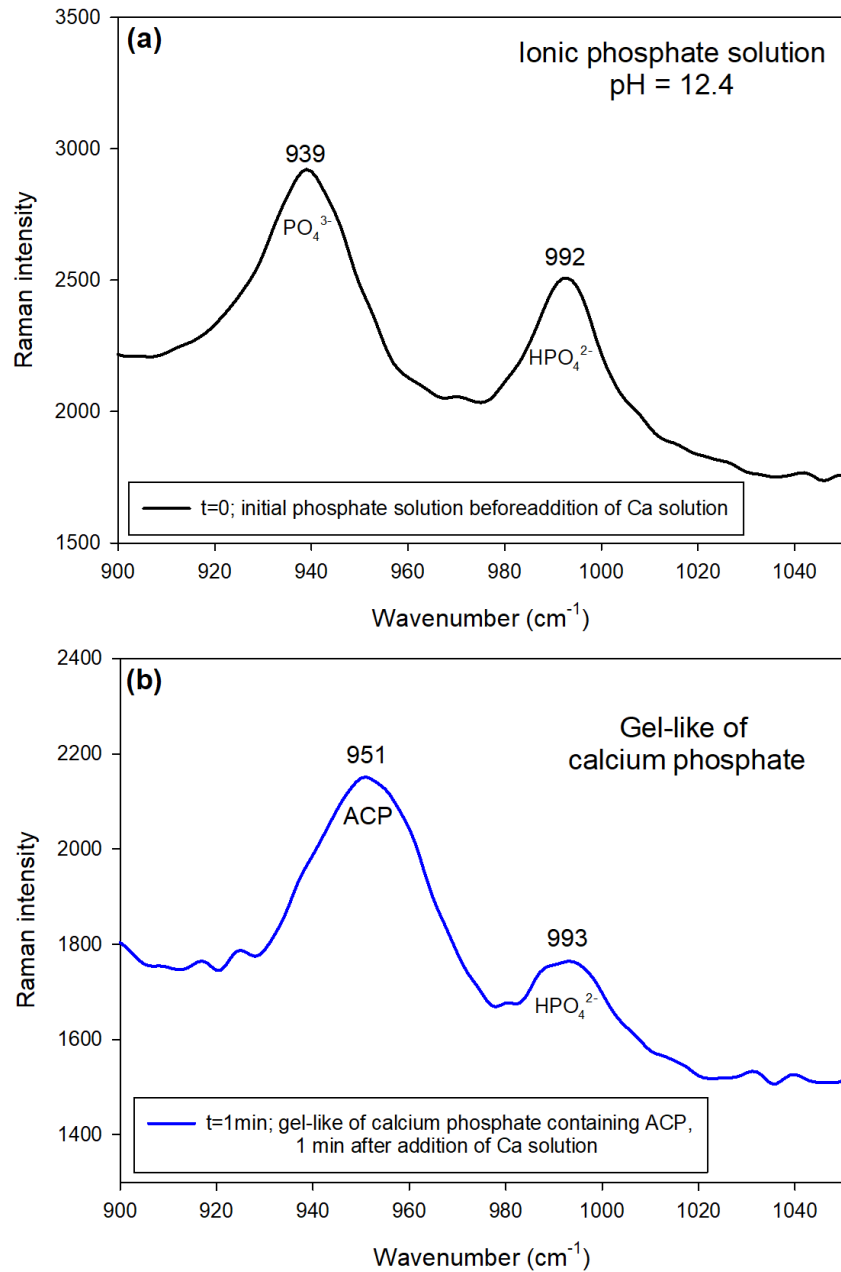
Figure S2: (top) Initial Ca(OH)$_2$ slurry characterized *in situ* by a Raman peak at 362 cm^{-1} before the addition of a phosphate solution (experiment 3, Table 1). (bottom) Temporal evolution of the dissolution of calcium hydroxide during the formation of calcium phosphates.

Figure S3: (a) Characterization of the initial phosphate solution by Raman spectroscopy (experiment 7). (b) *In situ* Raman spectrum of the gel-like phase formed after one minute after injection of a calcium solution. The gel contains ACP and residual aqueous Ca-phosphate species (experiment 5, Table 1).
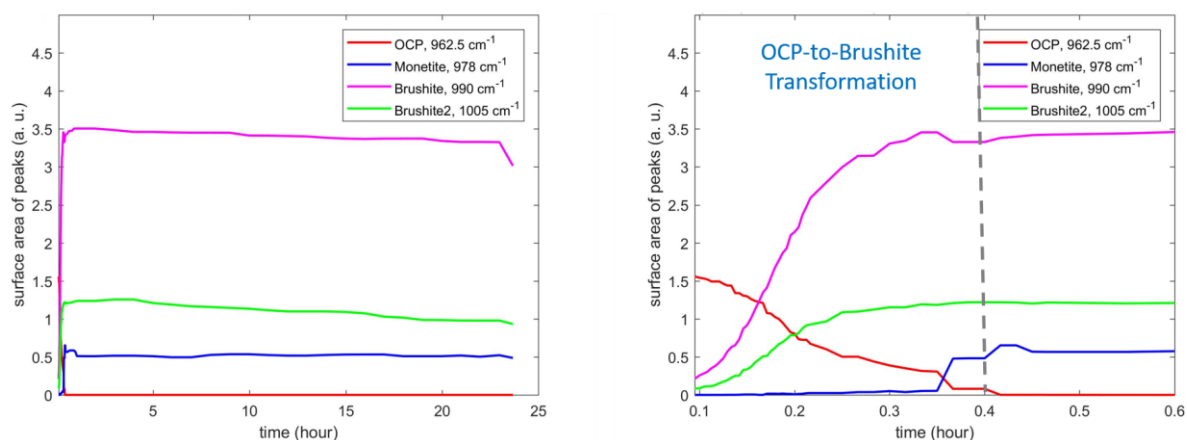
Figure S4: Temporal evolution of the integrated surface areas of selected peaks in the time-lapse Raman data in experiment 1. Left: time evolution of the peak surface areas (considered as proxies for concentration in the suspension) of octo-calcium phosphate (OCP), brushite (two vibration modes at 990 and 1005 cm^{-1}) and monetite. Monetite peak is not clearly detected the *in situ* Raman data or in the ex-situ DRX analyses, but it is required to improve the deconvolution of the peaks during the fitting procedure. ACP is excluded in the fit because it is only present in the first two minutes. Right: zoom of the left figure between 0.1 and 0.6 hours showing the nucleation of brushite and monetite. The different Raman peaks are calculated using a numerical fitting procedure shown on Movie S1.
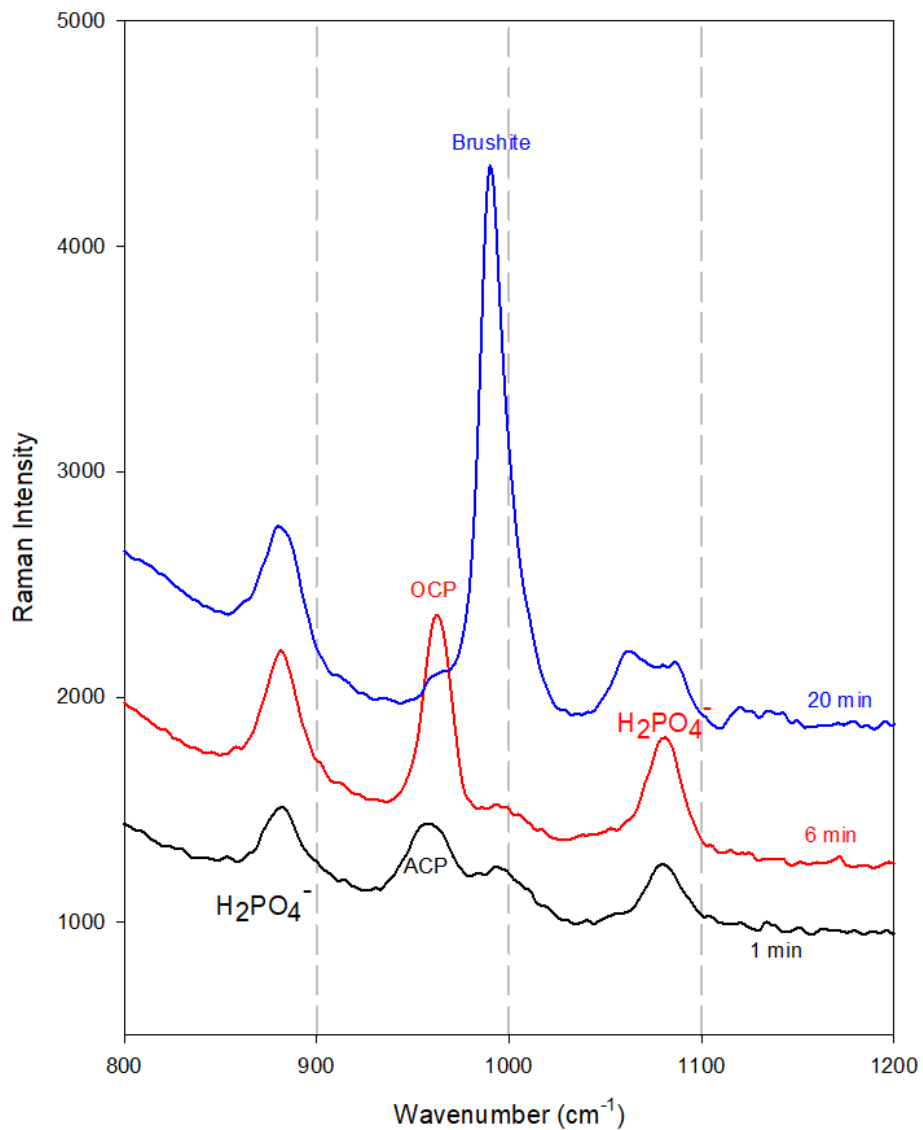
Figure S5: Raman spectra after 1 minute (black), 6 minutes (red) and 20 hours (blue) in experiment 1 (Table 1) showing that the formation of ACP and its transformation into OCP implies the production of $H_2PO_4^-$. This result supports the reaction 4 described in the main text.
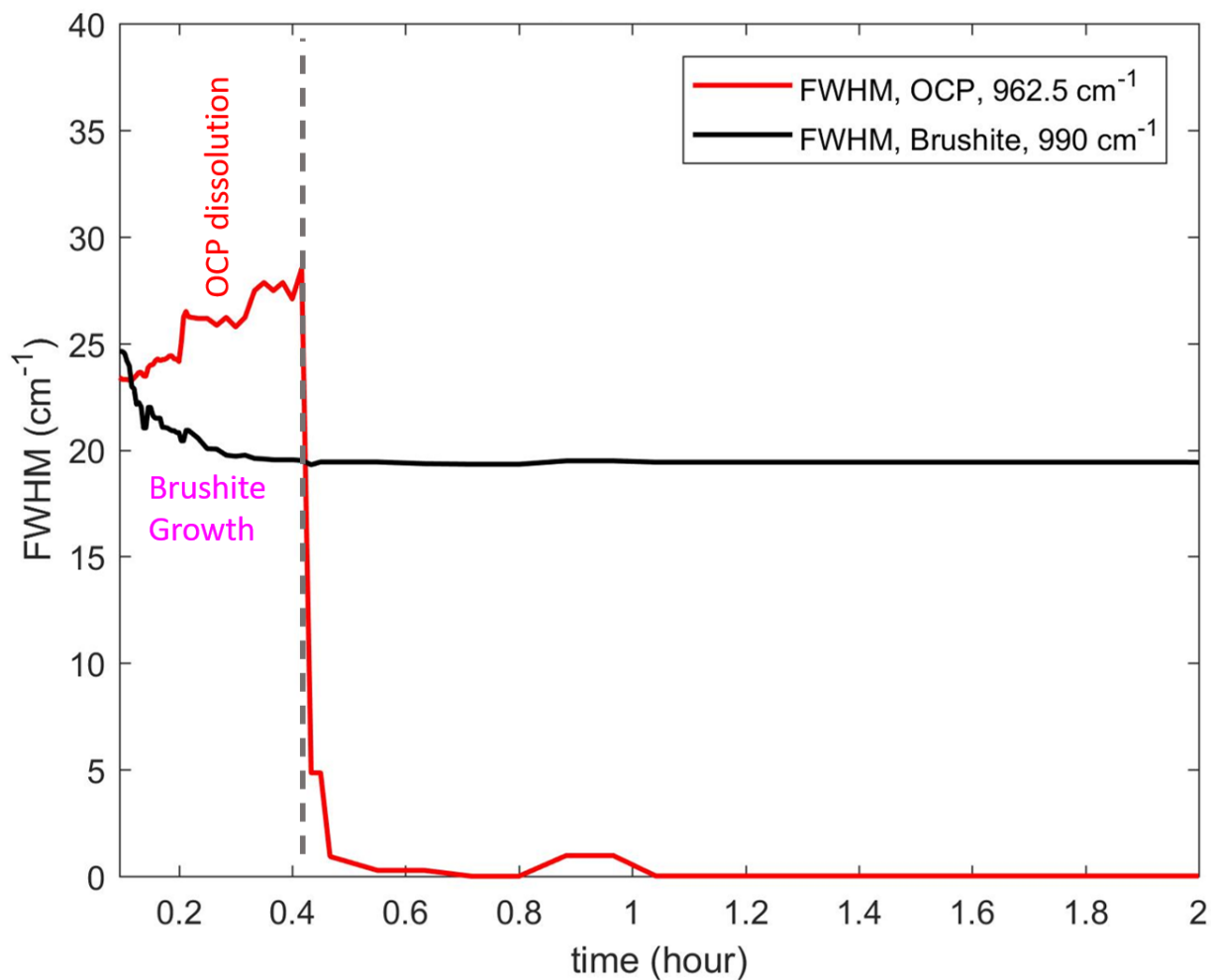
Figure S6. Transformation of OCP into brushite via a dissolution-recrystallization pathway in experiment 1 (Table 1). A temporal increase of the FWHM of OCP (dissolution process because the crystal size is proportional to $1/\text{FWHM}_{OCP}$) is coupled to a temporal decrease of FWHM for brushite (growth process).

20 µm

Micro-crystals of brushite, CaHPO4.2H2O (exp. 1)

Figure S7: FESEM image showing elongated micro-crystals of brushite (size > 20µm) obtained in experiment 1 (Table 1).
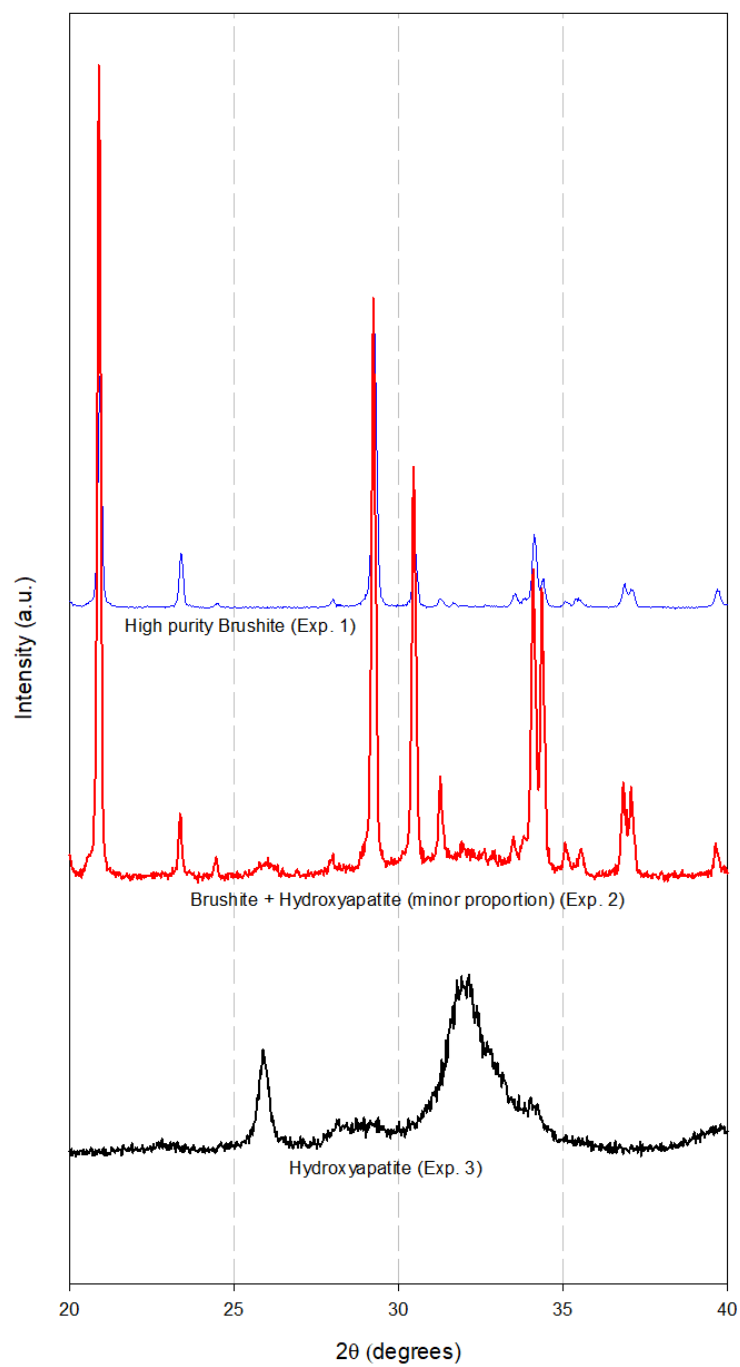
Figure S8. X-ray diffraction data acquired on recovered solid products collected after experiments 1, 2 and 3 (Table 1).
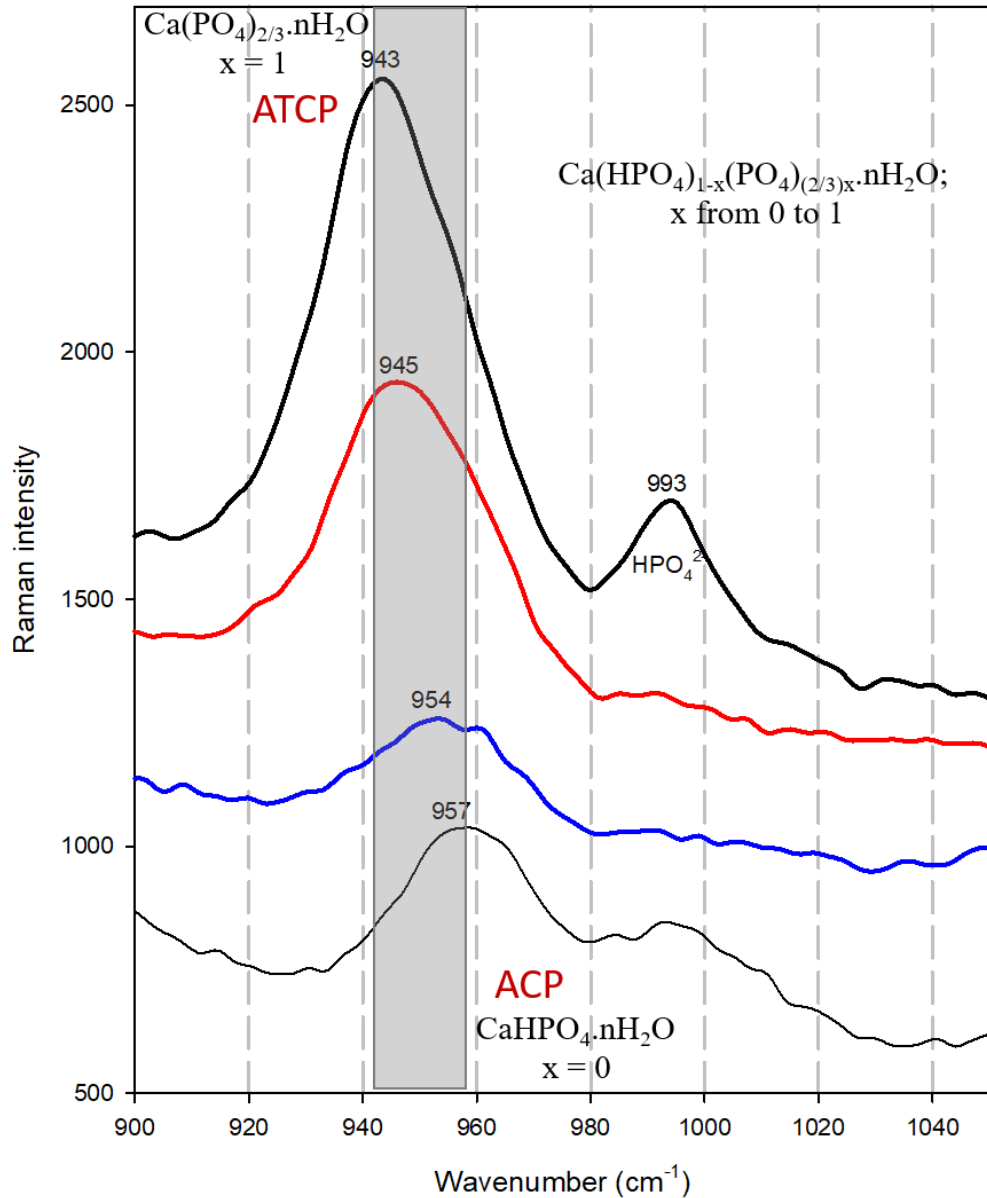
Figure S9. Four different Raman signatures of amorphous calcium phosphate phases detected in experiments 1 and 3 (Table 1). The position of the main Raman peak of amorphous calcium phases varies between 943 cm^{-1} (Ca(PO$_4$)$_{2/3}$.nH$_2$O) and 957 cm^{-1} (for CaHPO$_4$.nH$_2$O) . A linear interpolation is assumed to calculate the phosphate content (x=68.357 − (1/14)*P$_{ACP}$: where P$_{ACP}$ is the position in cm^{-1} comprised between 943 and 957).
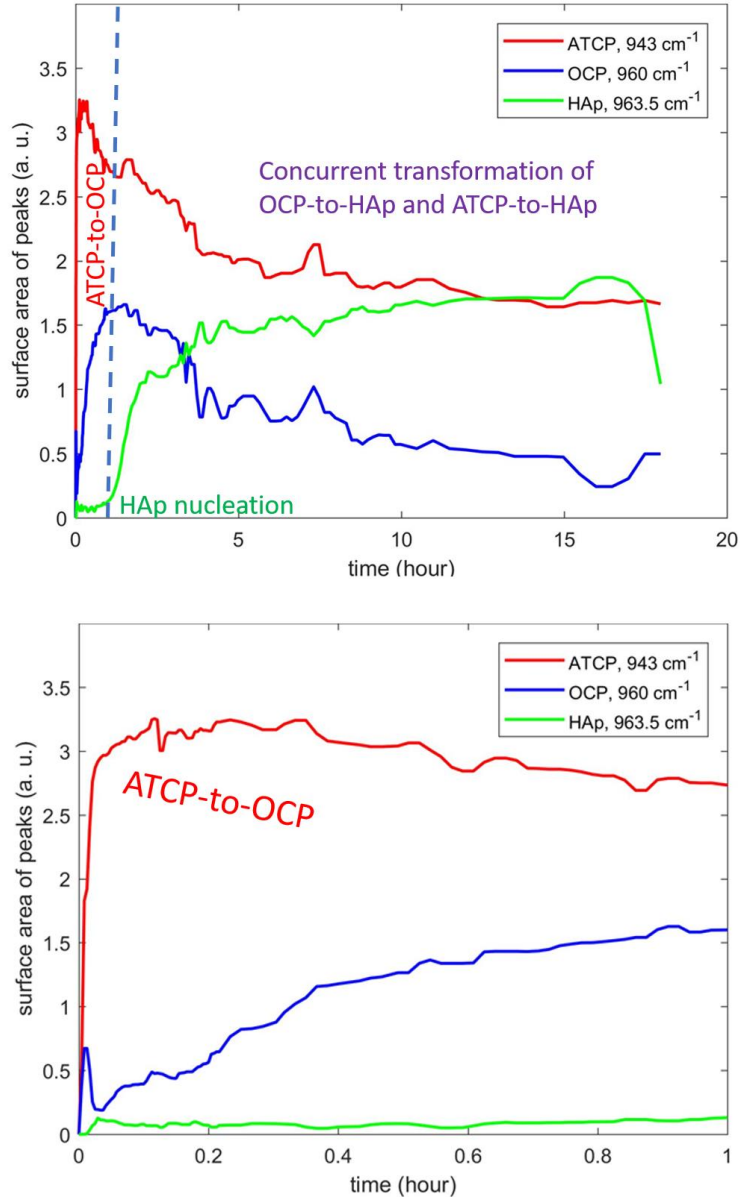
Figure S10: Temporal evolution of the integrated surface areas of selected Raman peaks in experiment 3 (Table 1). Top: time evolution of the peak surface areas, considered as proxies for concentration in the suspension, of amorphous tricalcium phosphate (ATCP), octo-calcium phosphate (OCP) and hydroxyapatite (HAp). ACP1 was excluded in the fit because it was only present in the first two minutes. Bottom: zoom of the top figure between 0 and 1 hour showing the transformation of ATCP into OCP. The different Raman peaks are calculated using a fitting procedure shown on Movie S2.
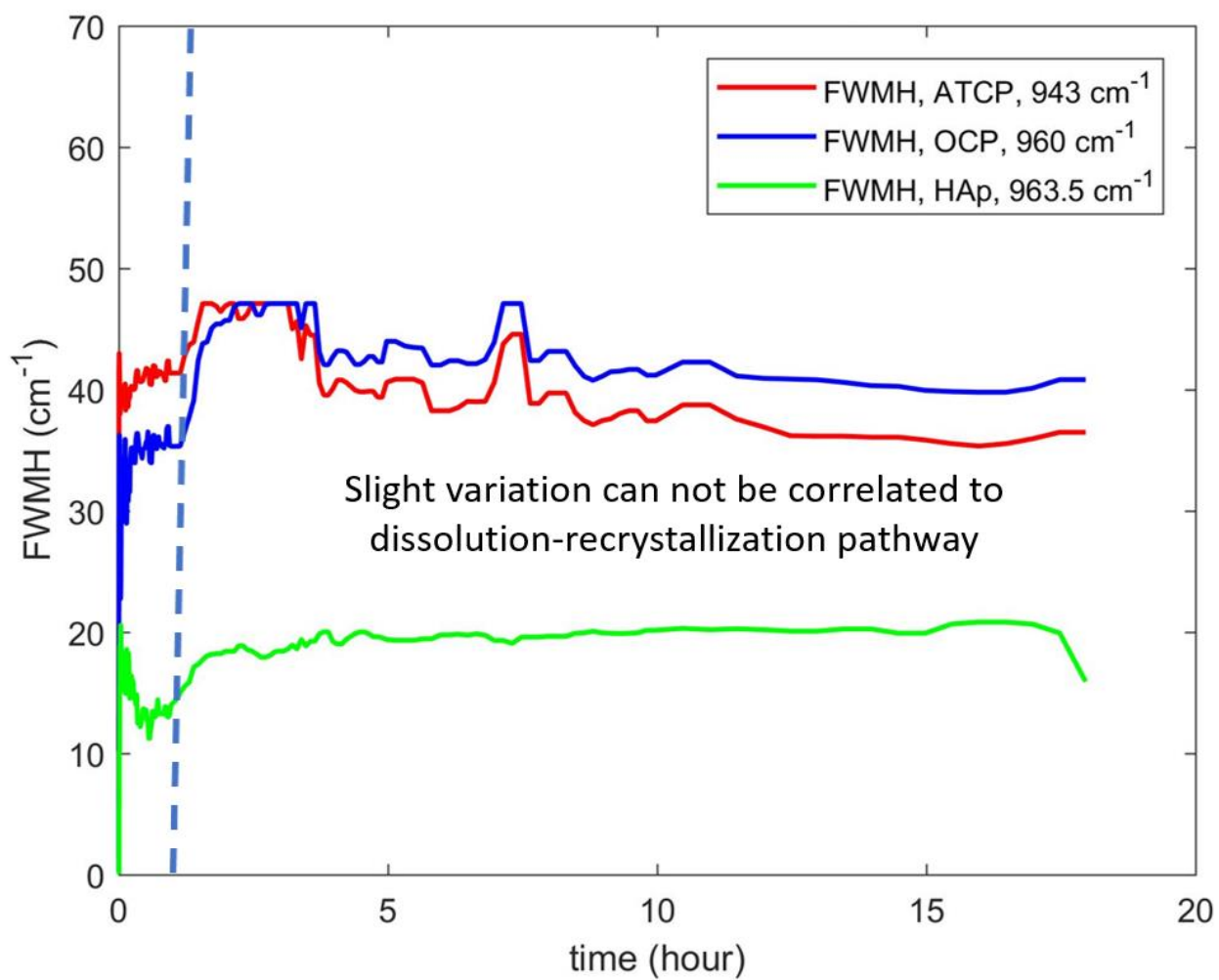
49

Figure S11. Temporal behavior of FWHM parameter for ATCP, OCP and hydroxyapatite (HAp) during formation of HAp in high alkaline medium in experiment 3 (Table 1). Assuming that the crystal size is proportional to 1/FWHM, here the data to not allow to conclude if a dissolution-crystallization pathway is a dominant process or if only partial dissolution occurs, as explained in the text.
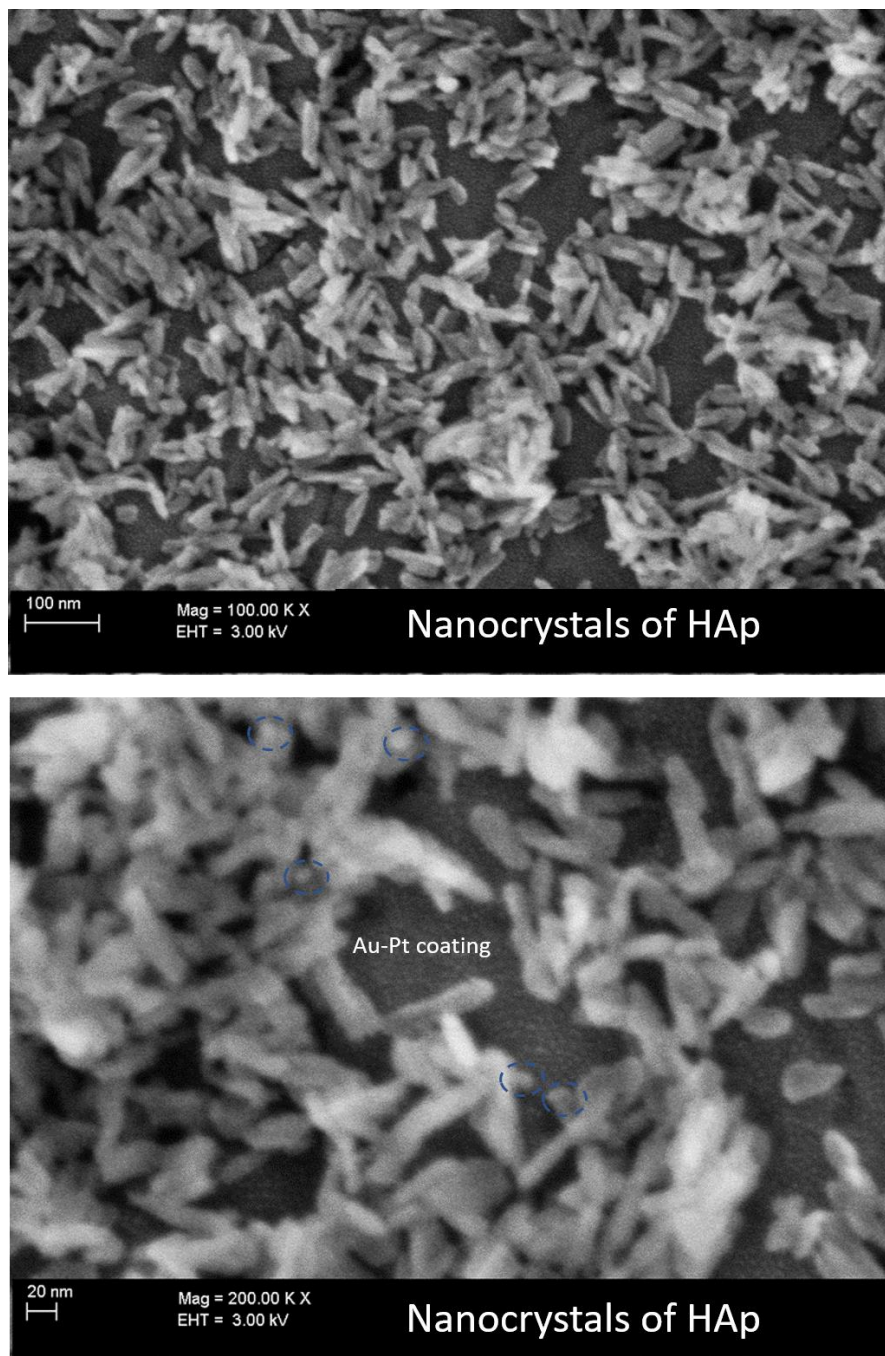
Figure S12: FESEM images showing acicular nanocrystals of hydroxyapatite (HAp) (size<100nm) obtained in experiment 3 (Table 1).
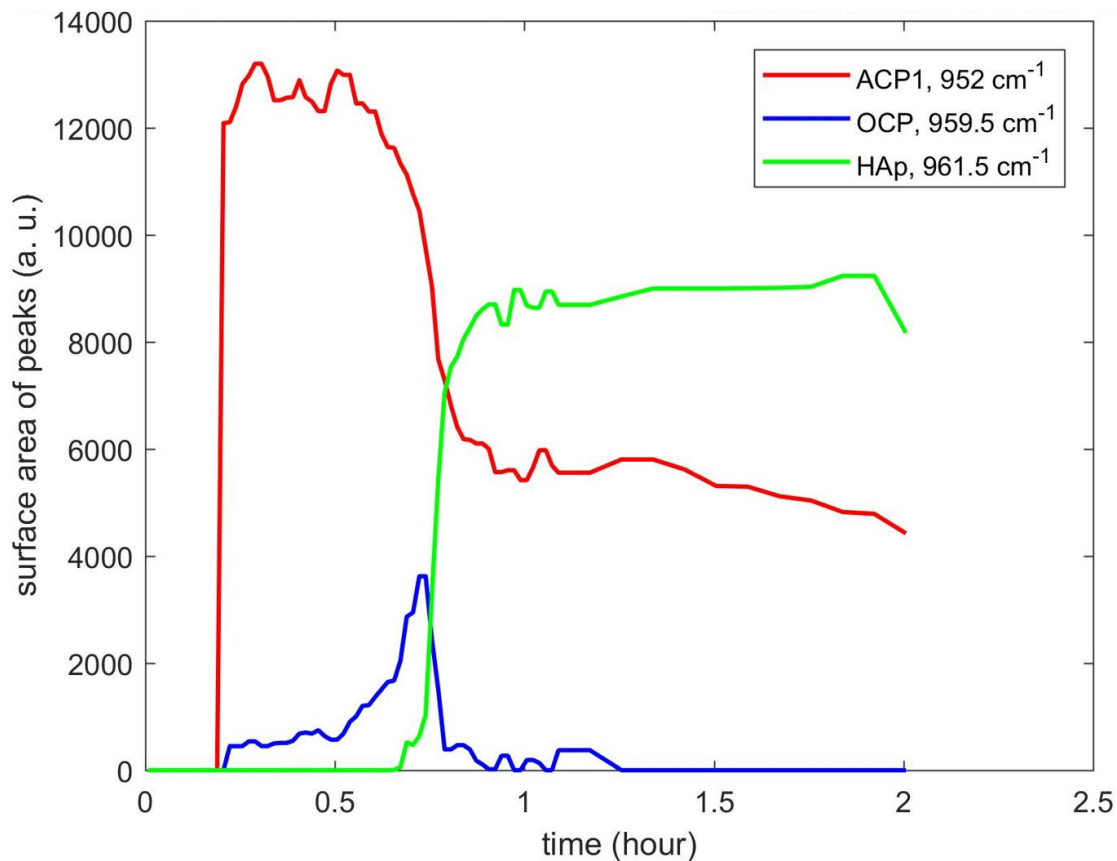
Figure S13. Temporal evolution of the integrated surface areas of selected Raman peaks in experiment 5 (Table 1). The figure displays the peak surface areas, considered as proxies for concentration in the suspension, of amorphous calcium phosphate (ACP1), octo-calcium phosphate (OCP) and hydroxyapatite (HAp).
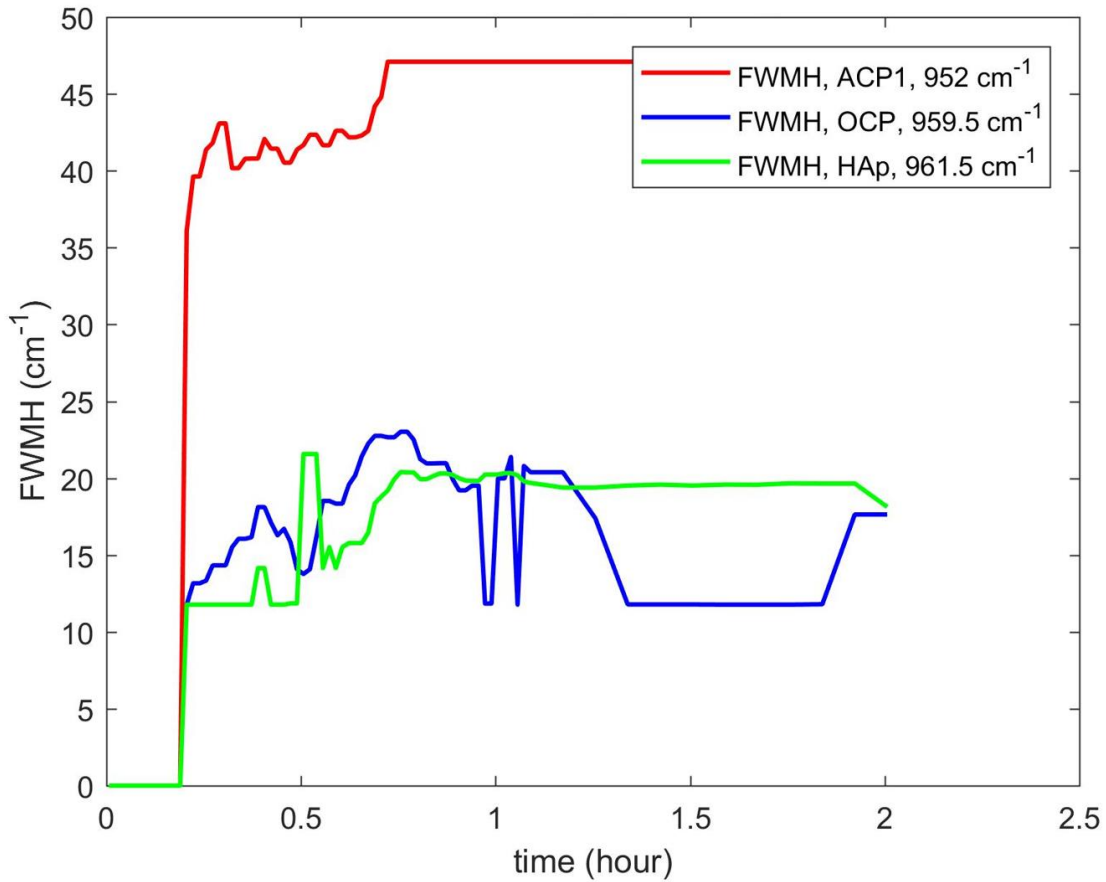
Figure S14. Temporal behavior of FWHM parameter for ACP1, OCP and hydroxyapatite (HAp) during formation of HAp in alkaline medium in experiment 5 (Table 1). Assuming that the crystal size is proportional to 1/FWHM, the data do not allow to conclude if a dissolution-crystallization pathway is a dominant process or if only partial dissolution occurs, as explained in the text.

Movie S1: Fit of the time-lapse Raman spectra of experiment 1 (Table 1) with four Gaussian curves corresponding to four different species. The time-lapse evolutions of the peak surface areas and FWHM displayed in the Figures S4 and S6 are calculated from this fit. The black curve represents the experimental data and the dashed cyan curve shows the nonlinear fit using the four Gaussian.

Movie S2: Fit of the time-lapse Raman spectra of experiment 3 (Table 1) with three Gaussian curves corresponding to three different species. The time-lapse evolutions of peak surface areas and FWHM displayed in the Figures S10 and S11 are calculated from this fit. The black curve represents the experimental data and the dashed cyan curve shows the nonlinear fit using the four Gaussian.

Movie S3: Fit of the time-lapse Raman spectra of experiment 5 (Table 1) with three Gaussian curves corresponding to three different species. The time-lapse evolutions of peak surface areas and FWHM displayed in the Figures S13 and S14 are calculated from this fit. The black curve represents the experimental data and the dashed cyan curve shows the nonlinear fit using the four Gaussian.